

# Real-Time Parameter Estimation for Flexible Aircraft

Jared A. Grauer\*

*NASA Langley Research Center, Hampton, Virginia, 23681*

and

Matthew J. Boucher†

*NASA Armstrong Flight Research Center, Edwards, California, 93523*

A method for estimating aeroelastic stability and control derivatives for flexible aircraft is developed and demonstrated using flight test data for the X-56A subscale demonstrator. The method uses the equation-error approach with frequency-domain data, and can be applied post-flight or in real time during flight. The nondimensional aeroelastic forces and moments and the explanatory variables (including generalized displacement, rate, and acceleration states for the vibration modes) are estimated using a finite element model and onboard sensor measurements in both a least squares and Kalman filtering framework. The data are then transformed into the frequency domain for parameter estimation using equation error. This method can result in a more efficient analysis than with other iterative methods, and can leverage existing statistical tools for model structure determination, data collinearity detection, combining multiple maneuvers or prior information, and others to improve model quality.

## Nomenclature

$C_D, C_Y, C_L$	stability-axis force coefficients	$\phi, \theta, \psi$	Euler angles, rad
$C_{D_w}, C_{Y_w}$	wind-axis force coefficients	$\mu$	flank angle, rad
$C_l, C_m, C_n$	body-axis moment coefficients	$\sigma$	standard deviation
$C_Q$	generalized modal force coefficients	<b>Subscripts</b>	
$\bar{c}$	mean aerodynamic chord, ft	$eq$	equivalent value
$j$	imaginary number, $= \sqrt{-1}$	<b>Superscripts</b>	
$p, q, r$	angular rates, rad/s	$^{-1}$	matrix inverse
$\bar{q}$	dynamic pressure, lbf/ft <sup>2</sup>	$T$	transpose
$\Re$	real part	$\cdot$	time derivative
$S$	wing reference area, ft <sup>2</sup>	$\dagger$	complex conjugate transpose
$x, y, z$	body-axis coordinates, ft	$\wedge$	estimated value
$\Delta t$	sampling interval, s	$\sim$	error
$\alpha$	angle of attack, rad		
$\beta$	sideslip angle, rad		
$\delta$	control surface deflection, rad		

\*Research Engineer, Dynamic Systems and Control Branch, MS 308, Senior Member AIAA.

†Research Engineer, Controls and Dynamics Branch, MS 4840D, Member AIAA.

## I. Introduction

THE recent resurgence of interest in flexible aircraft is in part due to the potential improvements in fuel economy, aerodynamic efficiency, range and endurance, noise reduction, ride quality, and other performance metrics. For example, the NASA Advanced Air Transport Technology (AATT) Project currently aims to mature modeling and control technologies using the X-56A Multi-Utility Technology Testbed (MUTT) for active flutter suppression and gust load alleviation [1]. System identification and parameter estimation can support this goal by supplying aerodynamic models identified from flight test data to verify existing simulation models and update aerodynamic databases for flight control design.

Although examples of system identification for flexible aircraft are relatively few [2], recent works [3–6] have all employed the model proposed in Ref. [7], which extended flight dynamics models based on quasi-steady stability and control derivatives to flexible aircraft. One reason for this comparatively small number of system identification examples could be the relative difficulty in identifying aeroelastic systems. To start, the dynamic models are significantly larger and more complex than for traditional aircraft. If nonlinear estimators are used, such as the output-error approach [8, 9], good starting values are needed for the many unknown parameters to achieve convergence. Although rigid-body derivatives may be predicted well using traditional analysis or experiment, the numerous aeroelastic coupling derivatives are less intuitive and may require a numerical aerodynamic analysis with a finite element model (FEM) for prediction. Also, determining which model parameters should be included in the model requires time-consuming iteration. For flight test, numerous additional sensors, and sometimes actuators, are needed to observe the aeroelastic interactions, thereby increasing the cost and complexity of the test aircraft. Additionally, longer data records and more careful experiment designs are needed to collect enough information to accurately estimate each of the important aeroelastic derivatives.

With few exceptions, the equation-error approach for parameter estimation has seldom been applied to flexible aircraft. One explanation for this is that equation error requires accurate measurements of the aeroelastic forces and moments and the explanatory variables; however, mean-axis and structural states are confounded together in the sensor measurements and not easily separated for analysis [10, 11]. In addition, many structural modes can participate in the aircraft response, which requires many redundant and distributed sensors and actuators to gain sufficient resolution on the vibration modes.

Turning this problem around, if information on the structural states could be reconstructed from sensor measurements, then the forces, moments, and explanatory variables could be obtained for use in an equation-error analysis. The advantage of this approach is that the solution for the optimal parameter estimates is deterministic and does not require iteration or good starting values, which leads to a more efficient analysis. Additionally, forces and moments are examined separately, instead of at the same time, which helps to break the modeling task into smaller, more manageable parts. Many tools from regression analysis are available to the analyst, such as for model structure determination, data collinearity detection, and sensitivity analysis. Applied in the frequency domain, equation error automatically rejects noise and removes bias parameters, which improves results and simplifies the estimation problem. Furthermore, applying equation error in the frequency domain enables real-time estimation, which can provide modeling results during flight, predict flutter, monitor stability margins during envelope expansion tests, and judge maneuver quality.

This paper presents a framework for applying equation error with flexible aircraft in both batch and real-time analyses. Least-squares estimators are used to estimate generalized modal displacements, rates, and accelerations from relevant onboard sensor data. A Kalman filter is then applied to improve these estimates and enforce kinematic consistency. Afterwards, aeroelastic forces and moments and the explanatory variables are computed from measured data for estimation using equation-error. Section II describes the equation-error method for estimating model parameters using frequency-domain data, both as a batch, post-flight procedure and in real time during flight. Section III introduces the flexible aircraft model used for system identification. Section IV presents the method for reducing the measurements to enable estimation with equation error. Next, Section V describes the X-56A airplane and flight tests, with identification results presented in Section VI. Concluding remarks are given in Section VII.

Due to ITAR restrictions associated with the X-56A airplane, numerical values are not given in this paper; however, the method is general and not specific to the X-56A airplane. Computer software for the multisine input design, Fourier transforms, model structure determination, and both batch and real-time equation-error parameter estimation used are available in a MATLAB<sup>®</sup> toolbox called System IDentification Programs for AirCraft [12], which is associated with Ref. [9].

## II. Parameter Estimation

### II.A. The Equation-Error Approach

This section briefly summarizes the equation-error method for parameter estimation, using frequency-domain data. For more information on the method, see Refs. [9,13]. The equation-error method results from simplifying the Maximum Likelihood estimator for the case when there is process noise but no measurement noise. In this case the estimation reduces to the least-squares problem

$$\mathbf{z} = \mathbf{X}\boldsymbol{\theta} + \mathbf{v} \quad (1)$$

The variable  $\mathbf{z}$  is a vector of measured or computed data to be modeled. The regressor matrix  $\mathbf{X}$  assembles column vectors of explanatory variables. The vector  $\boldsymbol{\theta}$  contains the unknown model parameters. Lastly,  $\mathbf{v}$  is a vector of equation errors that are assumed to be zero mean, normally distributed, and spectrally white.

The ordinary least squares cost function

$$J(\boldsymbol{\theta}) = \frac{1}{2} (\mathbf{z} - \mathbf{X}\boldsymbol{\theta})^\dagger (\mathbf{z} - \mathbf{X}\boldsymbol{\theta}) \quad (2)$$

is the sum of squared errors between the data and the model output for that data. The optimal solution for the model parameters is

$$\hat{\boldsymbol{\theta}} = [\Re(\mathbf{X}^\dagger \mathbf{X})]^{-1} \Re(\mathbf{X}^\dagger \mathbf{z}) \quad (3)$$

with covariance

$$\text{cov}(\hat{\boldsymbol{\theta}}) = \sigma^2 [\Re(\mathbf{X}^\dagger \mathbf{X})]^{-1} \quad (4)$$

where  $\sigma^2$  is the equation-error variance. The equation-error variance  $\sigma^2$  is usually estimated from the model residuals as

$$\hat{\sigma}^2 = \frac{\mathbf{v}^\dagger \mathbf{v}}{N - n_p} \quad (5)$$

where  $N$  is the number of data points and  $n_p$  is the number of parameters.

Least squares is applied several times in this paper because it is a simple and accurate estimator when assumptions are valid. Furthermore, the solution to the least-squares problem is analytic and closed-form. This is in contrast to nonlinear estimators, which require iteration and are not well-suited for real-time applications. One drawback to using equation error is that all the explanatory variables must be available, which is difficult in analysis of flexible aircraft.

### II.B. Real-Time Estimation in the Frequency Domain

Equation error, as just summarized, is formulated for batch estimation after a flight test maneuver has completed and all the data are available. This section summarizes simple changes to the method that facilitate real-time estimation in the frequency domain. For more information on this technique, see Refs. [9,14].

For batch, post-flight estimation, a high-accuracy Fourier transform is used to transform the measured data into the frequency domain. During real-time estimation, however, a simplified transform is used. The signal  $z(t)$ , for example, over the time interval  $t \in [0, T]$  has the following approximation to the finite Fourier transform

$$\mathcal{F}\{z(t)\} \triangleq z(j\omega_k) = \Delta t \sum_{i=0}^{N-1} z(t_i) e^{-j\omega_k t_i} \quad (6)$$

for equally-spaced time samples  $t_i$  and selected analysis frequencies  $\omega_k$ . The regressor matrix is transformed similarly.

This estimation can also be performed in real time, as the aircraft is flying, using a recursive version of the Fourier transform. Expanding Eq. (6) and regrouping terms, the transform at any time  $t_i$  can be written as the recursive relation

$$z_i(j\omega_k) = z_{i-1}(j\omega_k) + z(t_i) e^{-j\omega_k t_i} \Delta t \quad (7)$$

As data are collected, the Fourier transforms of  $\mathbf{z}$  and  $\mathbf{X}$  are updated recursively in real time. Then the least squares solution Eq. (3) and its covariance Eqs. (4)–(5) are computed. If computational resources are

limited, the least-squares solution can be calculated at a slower rate, with the only potential drawback that modeling results are updated less often.

If flight conditions or parameters are changing over time, data forgetting techniques can be used to devalue older data and adapt more quickly to newer data. A simple method for this is exponential forgetting, where the recursive Fourier transform is modified as

$$z_i(j\omega_k) = \lambda z_{i-1}(j\omega_k) + z(t_i) e^{-j\omega_k t_i} \Delta t \quad (8)$$

where  $\lambda$  is the forgetting factor, typically selected between 0.9 and 1.0.

### III. Flexible Aircraft Model

This section describes the aeroelastic flight dynamics model used for a flexible aircraft. The model is based on Ref. [7] with further elaboration in Ref. [10], and is briefly summarized here. First, the deformation of the aircraft structure is parameterized in terms of a finite set of orthogonal vibration modes. Second, the nondimensional forces and moments acting on the aircraft are expanded in terms of stability and control derivatives.

#### III.A. Structural Deformations

The deformation of the aircraft structure is assumed to be small and within the linear elastic range. As such, each vibration mode deforming the structure about the aircraft mean axes can be approximated as the second-order system

$$\ddot{\eta}_i + 2\zeta_i \omega_i \dot{\eta}_i + \omega_i^2 \Delta \eta_i = \frac{\bar{q} S \bar{c}}{m_i} C_{Q_i} \quad (9)$$

The terms  $\eta_i$ ,  $\dot{\eta}_i$ , and  $\ddot{\eta}_i$  are the generalized displacement, rate, and acceleration of the  $i^{th}$  vibration mode. The modal constants  $m_i$ ,  $\omega_i$ , and  $\zeta_i$  are the generalized mass, frequency, and damping ratio. The nondimensional generalized force coefficient  $C_{Q_i}$  quantifies the forcing on the vibration mode. Note the adjective “modal” is used in this paper to reference the vibration modes and not, for example, the short period flight dynamics mode.

The deformation of an arbitrary point on the aircraft from its undeformed jig shape is parameterized using the mode shapes and modal displacements as

$$\begin{aligned} \mathbf{d}(\mathbf{r}, t) &= \sum_{k=1}^M \phi_k(\mathbf{r}) \eta_k(t) \\ &= \phi_1 \eta_1 + \phi_2 \eta_2 + \dots + \phi_M \eta_M \\ &= \phi_k \eta_k \end{aligned} \quad (10)$$

The vector  $\mathbf{r}$  is the local body-fixed position of a point relative to the aircraft mass center. The vector  $\phi_k$  is the local mode shape describing the spatial displacement of  $\mathbf{r}$  due to a unit displacement of  $\eta_k$ . Although in theory an infinite number of vibration modes exist, only a finite set of  $M$  modes is considered in practice. The last line of Eq. (10) shows how Einstein notation is used in this paper to economically represent sums of modal contributions, where terms indexed by  $k$  are to be evaluated and summed from 1 to  $M$ .

The vibration modes describe free vibrations of the aircraft structure in a vacuum. The modal masses, frequencies, damping ratios, and mode shapes may be obtained from a FEM and/or a ground vibration test (GVT). These parameters are a function of the the layout and composition of the aircraft, and may need to be scheduled according to other parameters, such as fuel weight. Although in flight the vibration modes couple together as a function of dynamic pressure, they are an advantageous choice of basis functions for expressing the structural deformation because they have physical significance and familiarity, can be measured or modeled, and have useful orthogonality properties for flight dynamics analysis. The structural deformation models considered here are for small displacements and elastic vibration only. The mass distribution of the aircraft is also assumed to be not significantly affected by the deformations. When this is not the case, for example with high altitude long endurance (HALE) aircraft, more complex structural deformation models must be used.

The relative amplitudes of the modal displacement, rate, and acceleration are proportional to 1,  $\omega_i$ , and  $\omega_i^2$ , respectively [11]. For frequencies larger than 1 rad/s or about 0.16 Hz, which is the usual case for aircraft, the amplitudes of the modal states may differ by an order of magnitude or more. Therefore it will be assumed later that  $\eta_i < \dot{\eta}_i$  and  $\dot{\eta}_i < \ddot{\eta}_i$  to simplify equations.

### III.B. Aeroelastic Forces and Moments

The aeroelastic forces and moments acting on the aircraft were modeled using truncated Taylor series expansions in the aircraft states and controls. The aerodynamic force coefficients, expanded in the stability axes, are

$$C_D = C_{D_0} + C_{D_V} \frac{\Delta V}{V_0} + C_{D_\alpha} \Delta\alpha + C_{D_q} \frac{q\bar{c}}{2V_0} + C_{D_{\eta_k}} \Delta\eta_k + C_{D_{\dot{\eta}_k}} \frac{\dot{\eta}_k \bar{c}}{2V_0} + C_{D_\delta} \Delta\delta \quad (11a)$$

$$C_Y = C_{Y_0} + C_{Y_\beta} \Delta\beta + C_{Y_p} \frac{pb}{2V_0} + C_{Y_r} \frac{rb}{2V_0} + C_{Y_{\eta_k}} \Delta\eta_k + C_{Y_{\dot{\eta}_k}} \frac{\dot{\eta}_k b}{2V_0} + C_{Y_\delta} \Delta\delta \quad (11b)$$

$$C_L = C_{L_0} + C_{L_V} \frac{\Delta V}{V_0} + C_{L_\alpha} \Delta\alpha + C_{L_q} \frac{q\bar{c}}{2V_0} + C_{L_{\eta_k}} \Delta\eta_k + C_{L_{\dot{\eta}_k}} \frac{\dot{\eta}_k \bar{c}}{2V_0} + C_{L_\delta} \Delta\delta \quad (11c)$$

the aerodynamic moment coefficients are

$$C_l = C_{l_0} + C_{l_\beta} \Delta\beta + C_{l_p} \frac{pb}{2V_0} + C_{l_r} \frac{rb}{2V_0} + C_{l_{\eta_k}} \Delta\eta_k + C_{l_{\dot{\eta}_k}} \frac{\dot{\eta}_k b}{2V_0} + C_{l_\delta} \Delta\delta \quad (12a)$$

$$C_m = C_{m_0} + C_{m_V} \frac{\Delta V}{V_0} + C_{m_\alpha} \Delta\alpha + C_{m_q} \frac{q\bar{c}}{2V_0} + C_{m_{\eta_k}} \Delta\eta_k + C_{m_{\dot{\eta}_k}} \frac{\dot{\eta}_k \bar{c}}{2V_0} + C_{m_\delta} \Delta\delta \quad (12b)$$

$$C_n = C_{n_0} + C_{n_\beta} \Delta\beta + C_{n_p} \frac{pb}{2V_0} + C_{n_r} \frac{rb}{2V_0} + C_{n_{\eta_k}} \Delta\eta_k + C_{n_{\dot{\eta}_k}} \frac{\dot{\eta}_k b}{2V_0} + C_{n_\delta} \Delta\delta \quad (12c)$$

and the generalized force coefficients in Eq. (9) are expanded as

$$\begin{aligned} C_{Q_i} = & C_{Q_{i_0}} + C_{Q_{i_V}} \frac{\Delta V}{V_0} + C_{Q_{i_\beta}} \Delta\beta + C_{Q_{i_\alpha}} \Delta\alpha + C_{Q_{i_p}} \frac{pb}{2V_0} + C_{Q_{i_q}} \frac{q\bar{c}}{2V_0} + C_{Q_{i_r}} \frac{rb}{2V_0} \\ & + C_{Q_{i_{\eta_k}}} \Delta\eta_k + C_{Q_{i_{\dot{\eta}_k}}} \frac{\dot{\eta}_k \bar{c}}{2V_0} + C_{Q_{i_\delta}} \Delta\delta \end{aligned} \quad (13)$$

where  $_0$  denotes a reference condition and  $\Delta$  a perturbation. Traditional decoupling of the aircraft longitudinal and lateral-directional dynamics was assumed in these models. The generalized force coefficients can also be decoupled, depending on the mode, if the structural properties of the aircraft are not significantly different about the axes. These aeroelastic forces and moments are similar to those for traditional rigid aircraft models, except they include contributions from the modal displacements and rates, which couple the structural deformation of the aircraft to the traditional rigid-body response.

## IV. Estimation of Modeling Variables

In Section II, Fourier transforms and the equation-error approach were summarized. In Section III, the structural model and aeroelastic forces and moments were defined. However, equation error is not immediately applicable for flexible aircraft modeling because the modal states are unknown and because the measurements contain modal contributions that must be separated to obtain the explanatory variables and nondimensional coefficients.

This section describes an algorithm for separating the measurements into the mean axes and modal contributions to facilitate accurate real-time estimation using the equation-error method in the frequency domain. Figure 1 shows a simplified block diagram of the algorithm. In the first step, up to three separate least-squares estimators are used to compute the modal displacements from strain and attitude data, modal rates from airdata and gyroscope measurements, and modal accelerations from gyroscope and accelerometer data. The nondimensional aerodynamic force coefficients are also determined from the third least squares estimation. Because a modal displacement, rate, and acceleration are related through derivatives, a Kalman filter

is then applied in the second step to improve the modal state estimates and enforce kinematic consistency. Afterwards, the modal contributions to the measurements are removed to yield the remaining explanatory variables. Lastly, the nondimensional generalized force coefficients and the nondimensional aerodynamic moment coefficients are computed. These computations operate recursively on the data and can be performed as a post-flight or real-time analysis. After this procedure, equation-error parameter estimation can proceed normally using the techniques from Section II.

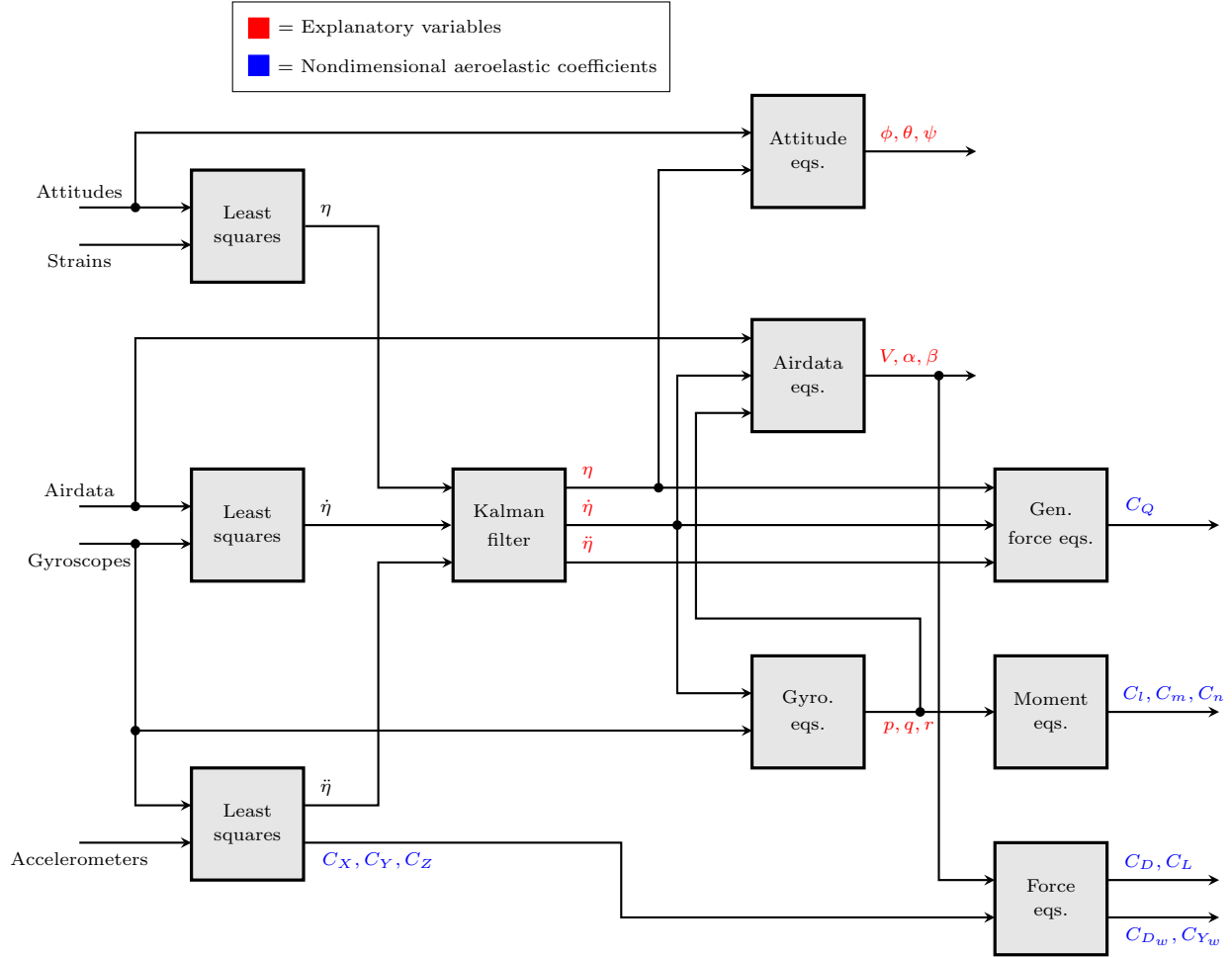


Figure 1. Simplified block diagram to estimate modeling variables from measurements and other data

#### IV.A. Estimating Modal Displacements

Strain data, and to a lesser extent attitude data, are the onboard measurements most affected by the modal displacements and therefore most useful in estimating these states. The output model for the strain data is [11]

$$\epsilon^i = \psi_k^i \eta_k + v^{\epsilon^i} \quad (14)$$

where  $i = 1, 2, \dots, n_\epsilon$  indicates the strain sensor index. This equation assumes linear deformations, temperature compensation, measurement noise  $v^{\epsilon^i}$ , and no systematic errors due to calibration or other factors. The terms  $\psi_k^i$  are the strain modes, which quantify the strain incurred at the  $i^{th}$  sensor by a unit displacement in  $\eta_k$  and can be obtained from a FEM solution.

Using many strain measurements at different points on the aircraft, a least-squares problem can be formed and solved for the unknown modal displacements. This concept is sometimes referred to as modal filtering.

Specifically, the data are assembled as

$$\begin{bmatrix} \epsilon^1 \\ \epsilon^2 \\ \vdots \\ \epsilon^{n_\epsilon} \end{bmatrix} = \begin{bmatrix} \psi_1^1 & \psi_2^1 & \dots & \psi_M^1 \\ \psi_1^2 & \psi_2^2 & \dots & \psi_M^2 \\ \vdots & \vdots & \ddots & \vdots \\ \psi_1^{n_\epsilon} & \psi_2^{n_\epsilon} & \dots & \psi_M^{n_\epsilon} \end{bmatrix} \begin{bmatrix} \eta_1 \\ \eta_2 \\ \vdots \\ \eta_M \end{bmatrix} + \begin{bmatrix} v^{\epsilon^1} \\ v^{\epsilon^2} \\ \vdots \\ v^{\epsilon^{n_\epsilon}} \end{bmatrix} \quad (15)$$

which is in the same form as the least-squares problem from Eq. (1), where the unknown parameters to be determined at each time step are

$$\boldsymbol{\theta} = \begin{bmatrix} \eta_1 & \eta_2 & \dots & \eta_M \end{bmatrix}^T \quad (16)$$

Although the strain modes vary with the inertia properties of the aircraft, these can usually be assumed constant for short durations of time so that  $(\mathbf{X}^T \mathbf{X})^{-1}$  need only be computed once for short maneuvers. Alternatively, the strain modes can be updated with current inertia information to enable accurate estimation over longer periods of time.

On one hand, the vibration modes included in Eq. (15) should be selected parsimoniously to avoid over-parameterizing the model and using unnecessary computation. On the other hand, as many modes as possible should be included to accurately capture the structural response. Mode selection can be performed automatically using an orthogonalization procedure [9]. Alternatively, this can be done iteratively through trial and error in a batch analysis, or the modes can be prescribed by the analyst during a real-time analysis. Because the strain modes are mutually orthogonal with respect to the modal mass matrix, correlated regressors are not typically an issue in this estimation.

Another issue is the number of sensors to include in the analysis. To obtain a least-squares solution for Eq. (15), at least one measurement is needed for each vibration mode considered in the analysis. More sensors may be needed, however, to improve the estimates or if some modes are not observable to some sensors. For reference, test articles for aeroelastic research commonly employ strain gauges on the order of 1 to 100. If fiber-optic strain sensors (FOSS) are used, the number of measurements can be on the order of 100 or 1000 per strand [15].

Attitude sensors provide the estimated orientation [11]

$$\phi^i = \phi + \nu_{k_\phi}^i \eta_k + v^{\phi^i} \quad (17a)$$

$$\theta^i = \theta + \nu_{k_\theta}^i \eta_k + v^{\theta^i} \quad (17b)$$

$$\psi^i = \psi + \nu_{k_\psi}^i \eta_k + v^{\psi^i} \quad (17c)$$

for  $i = 1, 2, \dots, n_\epsilon$ . The Euler angles  $\phi^i$ ,  $\theta^i$ , and  $\psi^i$  are the observed measurements, whereas  $\phi$ ,  $\theta$ , and  $\psi$  are the angles for the mean axis. The terms  $\nu_{k_\phi}$ ,  $\nu_{k_\theta}$ ,  $\nu_{k_\psi}$  are the gradients of the displacement mode shapes along the sensor axes for a particular sensor, and are often referred to as the modal slopes. If multiple attitude sensors are available, the least-squares problem Eq. (15) can be expanded to include the additional attitude equations, where now the unknown parameters to be estimated are

$$\boldsymbol{\theta} = \begin{bmatrix} \phi & \theta & \psi & \eta_1 & \eta_2 & \dots & \eta_M \end{bmatrix}^T \quad (18)$$

However, it is seldom that multiple attitude sensors are available, sampled at sufficient rates for aeroelastic analysis, and have good observability on the modes of interest. In these cases, the attitude data should not be included in the estimation to keep the dimension of the least-squares problem lower and save computational resources.

#### IV.B. Estimating Modal Rates

A similar process can be used to estimate the modal rates from multiple gyroscope and air-flow angle vanes. Neglecting systematic errors, these sensors have outputs [11]

$$p^i = p + \nu_{k_\phi}^i \dot{\eta}_k + v^{p_i} \quad (19a)$$

$$q^i = q + \nu_{k_\theta}^i \dot{\eta}_k + v^{q_i} \quad (19b)$$

$$r^i = r + \nu_{k_\psi}^i \dot{\eta}_k + v^{r_i} \quad (19c)$$

for  $i = 1, 2, \dots, n_g$ , and

$$\alpha^i = \alpha + \frac{p y_\alpha^i - q x_\alpha^i + \phi_{k_z}^i \dot{\eta}_k}{V} + v^{\alpha_i} \quad (20a)$$

$$\mu^i = \beta + \frac{r x_\mu^i - p z_\mu^i + \phi_{k_y}^i \dot{\eta}_k}{V} + v^{\mu_i} \quad (20b)$$

for  $i = 1, 2, \dots, n_v$ . Three-axis gyroscopes (for  $p$ ,  $q$ , and  $r$ ) and air-flow angle vane pairs (for  $\alpha$  and  $\mu$ ) are assumed here, but different numbers of each sensor can also be used. The terms  $\phi_{k_x}^i$ ,  $\phi_{k_y}^i$ , and  $\phi_{k_z}^i$  are the displacement mode shapes at each of the gyroscopes and vanes. The terms  $x$ ,  $y$ , and  $z$  indicate the body-axis locations of the undeformed angle of attack and flank angle sensors. The equations for angle of attack and flank or sideslip angle are linearizations that assume low aerodynamic flow angles, low angular rates, low modal rates, and high airspeeds, but are sufficient for most applications. Airspeed equations are not given because modal rates do not usually impact airspeed calculations to a significant degree, and because airspeed stability derivatives are typically negligible for subsonic flight and were not considered in this work. The second least-squares problem is then formed using Eqs. (19)–(20), where the unknown parameter vector to be estimated at each time step is

$$\boldsymbol{\theta} = \begin{bmatrix} p & q & r & \alpha & \beta & \dot{\eta}_1 & \dot{\eta}_2 & \dots & \dot{\eta}_M \end{bmatrix}^T \quad (21)$$

Again, for short, small perturbation maneuvers, the regressor matrix is essentially constant and can be computed once for the maneuver, or updated continuously for longer flight durations.

Estimating modal rates with this method requires redundant air-flow angle vanes and/or redundant gyroscopes because there are more than one unknown quantity in each measurement equation. It is common to have multiple airdata measurements, for example with airdata probes stemming from the wing tips or vertical tail, and also multiple gyroscopes from the use of multiple inertial measurement units or inertial navigation systems. However due to costs and maintenance issues, there are not usually many of these sensors, as there are with strain or accelerometer sensors. As a result, only a few structural modes can usually be estimated with this technique and it is more likely that modal rate information will be obtained from the Kalman filter output.

#### IV.C. Estimating Modal Accelerations

Accelerometers are the sensors most sensitive to the modal accelerations. Output equations for accelerometers are complex, nonlinear functions of the aircraft motion and deformation [11]. However, for most cases the modal displacements and rates are at least an order of magnitude smaller than the modal accelerations and can be neglected. Under these conditions and other mild assumptions, the outputs for accelerometers installed along the body axes of the undeformed aircraft are [11]

$$g a_x^i = \frac{\bar{q}S}{m} C_X + \frac{X_T}{m} - (q^2 + r^2) x_a^i + (pq - \dot{r}) y_a^i + (pr + \dot{q}) z_a^i + \phi_{k_x}^i \ddot{\eta}_k + v^{a_{x_i}} \quad (22a)$$

$$g a_y^i = \frac{\bar{q}S}{m} C_Y + (pq + \dot{r}) x_a^i - (p^2 + r^2) y_a^i + (qr - \dot{p}) z_a^i + \phi_{k_y}^i \ddot{\eta}_k + v^{a_{y_i}} \quad (22b)$$

$$g a_z^i = \frac{\bar{q}S}{m} C_Z + (pr - \dot{q}) x_a^i + (qr + \dot{p}) y_a^i - (p^2 + q^2) z_a^i + \phi_{k_z}^i \ddot{\eta}_k + v^{a_{z_i}} \quad (22c)$$



for  $i = 1, 2, \dots, n_a$ . Three-axis accelerometers are assumed here but different numbers of accelerometers can also be used. The constant  $g$  is the acceleration due to gravity,  $X_T$  is the propulsive thrust aligned with the body  $x$ -axis, and  $x_a^i$ ,  $y_a^i$ , and  $z_a^i$  are the body-fixed positions of the accelerometer. Accelerometer outputs are usually calibrated in g-units, but here the  $g$  conversion factor remains on the left side for convenience. If needed, other components of thrust can be included.

Equation (22) can be rearranged to form a third least-squares problem for the unknown nondimensional aerodynamic force coefficients and modal accelerations as

$$g a_x^i - \frac{X_T}{m} + (q^2 + r^2) x_a^i - (pq - \dot{r}) y_a^i - (pr + \dot{q}) z_a^i = \frac{\bar{q}S}{m} C_X + \phi_{k_x}^i \ddot{\eta}_k \quad (23a)$$

$$g a_y^i - (pq + \dot{r}) x_a^i + (p^2 + r^2) y_a^i - (qr - \dot{p}) z_a^i = \frac{\bar{q}S}{m} C_Y + \phi_{k_y}^i \ddot{\eta}_k \quad (23b)$$

$$g a_z^i - (pr - \dot{q}) x_a^i - (qr + \dot{p}) y_a^i + (p^2 + q^2) z_a^i = \frac{\bar{q}S}{m} C_Z + \phi_{k_z}^i \ddot{\eta}_k \quad (23c)$$

Measured data is substituted in the left side of Eq. (23) and the unknown parameters

$$\boldsymbol{\theta} = \begin{bmatrix} C_X & C_Y & C_Z & \ddot{\eta}_1 & \ddot{\eta}_2 & \dots & \ddot{\eta}_M \end{bmatrix}^T \quad (24)$$

appearing on the right side of the equation are estimated at each time step. Unlike the analysis of traditional rigid-body models where a single accelerometer triad is used to compute the nondimensional aerodynamic force coefficients, these variables are instead estimated (simultaneously with the modal accelerations) using many accelerometers in the analysis of flexible aircraft because each of the accelerometer outputs contain contributions from the modal accelerations.

Unless modal rates were estimated, as in Section IV.B, data for the mean-axis angular rates  $p$ ,  $q$ , and  $r$  are not available and the gyroscope measurements need to be used instead. However, directly substituting these measurements introduces additional modal accelerations into the equation, as seen from differentiation of Eq. (19) with respect to time. Because the modal accelerations are to be estimated, the equations can simply be rearranged again as

$$\begin{aligned} g a_x^i - \frac{X_T}{m} + [(q^j)^2 + (r^j)^2] x_a^i - (p^j q^j - \dot{r}^j) y_a^i - (p^j r^j + \dot{q}^j) z_a^i \\ = \frac{\bar{q}S}{m} C_X + (\phi_{k_x}^i + \nu_{k_\psi}^j y_a^i - \nu_{k_\theta}^j z_a^i) \ddot{\eta}_k + v^{a_{x_i}} \end{aligned} \quad (25a)$$

$$\begin{aligned} g a_y^i - (p^j q^j + \dot{r}^j) x_a^i + [(p^j)^2 + (r^j)^2] y_a^i - (q^j r^j - \dot{p}^j) z_a^i \\ = \frac{\bar{q}S}{m} C_Y + (\phi_{k_y}^i - \nu_{k_\psi}^j x_a^i + \nu_{k_\phi}^j z_a^i) \ddot{\eta}_k + v^{a_{y_i}} \end{aligned} \quad (25b)$$

$$\begin{aligned} g a_z^i - (p^j r^j - \dot{q}^j) x_a^i - (q^j r^j + \dot{p}^j) y_a^i + [(p^j)^2 + (q^j)^2] z_a^i \\ = \frac{\bar{q}S}{m} C_Z + (\phi_{k_z}^i + \nu_{k_\theta}^j x_a^i - \nu_{k_\phi}^j y_a^i) \ddot{\eta}_k + v^{a_{z_i}} \end{aligned} \quad (25c)$$

for the  $i^{th}$  accelerometer triad and using the  $j^{th}$  gyroscope. The modal acceleration contributions introduced by the measured angular accelerations are subsumed with those from the accelerometers on the right side. Again, for short, small perturbation maneuvers, the regressor matrix is essentially constant and can be computed once or updated at each time step for longer maneuvers.

#### IV.D. Kalman Filtering to Improve the Modal State Estimates

The three least-squares estimators discussed in Sections IV.A–IV.C estimate the modal displacements, rates, accelerations, and their uncertainties at each sample time, depending on the measurements available. These estimates, which are related by time derivatives, may be improved by enforcing kinematic constraints via a Kalman filter. Similar to the least-squares estimators, the Kalman filter can be run either in a batch

post-flight manner or recursively for real-time estimation. The Kalman filter setup is presented in this section; more details on the filter equations and operation are in Ref. [16], for example.

The equations relating the modal states for each vibration mode can be written as a double integrator. The discrete-time, state-space model is

$$\begin{bmatrix} x_1[n+1] \\ x_2[n+1] \end{bmatrix} = \begin{bmatrix} 1 & \Delta t \\ 0 & 1 \end{bmatrix} \begin{bmatrix} x_1[n] \\ x_2[n] \end{bmatrix} + \begin{bmatrix} \frac{1}{2}\Delta t^2 \\ \Delta t \end{bmatrix} u[n] + \begin{bmatrix} \frac{1}{2}\Delta t^2 \\ \Delta t \end{bmatrix} w[n] \quad (26a)$$

$$\begin{bmatrix} y_1[n] \\ y_2[n] \end{bmatrix} = \begin{bmatrix} 1 & 0 \\ 0 & 1 \end{bmatrix} \begin{bmatrix} x_1[n] \\ x_2[n] \end{bmatrix} + \begin{bmatrix} v_1[n] \\ v_2[n] \end{bmatrix} \quad (26b)$$

The states  $x_1$  and  $x_2$  are the modal displacement and rate, the input  $u$  is the estimated modal acceleration, the outputs  $y_1$  and  $y_2$  are the modal displacement and rate,  $\Delta t$  is the sampling period, and  $n$  is the sample index. The process noise  $w$  arises from uncertainty in the acceleration estimates, and the covariance obtained from the least-squares analysis is used for the process noise covariance matrix  $\mathbf{Q}$ . Similarly, measurement noise  $v$  is due to uncertainty in the estimated modal displacements and rates, and the measurement noise covariance matrix  $\mathbf{R}$  consists of the covariances of the least-squares estimates. Because these covariances are based on the data, the filter does not require tuning. The unsteady Kalman filter should be implemented, rather than the steady-state filter, because the covariance matrices change at each time step.

In this setup, the estimated modal accelerations are integrated twice, and those predictions are corrected using the estimated modal displacements and rates. This idea is similar to how inertial navigation systems operate using accelerometer and GPS data, or how aircraft instrumentation errors are removed during a data compatibility analysis [9, 17].

Depending on what information is available for a specific aircraft, the Kalman filter configuration can be changed. For example, if only modal displacement and acceleration information are supplied, the filter still performs well and the modal rates come as a byproduct of the filtering. If only modal displacement or acceleration is supplied, significant high-frequency or low-frequency errors will result in the estimates, respectively. For a post-flight analysis, deconvolution techniques [18] can be applied to help recover the signals.

#### IV.E. Computing the Remnant Modeling Variables

A few final computations are needed to extract the remaining explanatory variables from the available data and to compute the nondimensional coefficients for modeling using equation error. The remaining explanatory variables are obtained by removing the modal contributions output by the Kalman filter from the measurements to yield the mean-axis attitude, angular rates, and air-flow angles. This is done by rearranging Eqs. (17), (19), (20), and (23), and then substituting data for the modal states.

The body-axis nondimensional force coefficients were estimated from accelerometer data in Section IV.C. For post-flight analysis, these coefficients could be revised using the improved modal states from the Kalman filter. The nondimensional aerodynamic force coefficients can also be computed in other coordinate frames, including the stability axes as

$$C_D = -C_X \cos \alpha - C_Z \sin \alpha \quad (27a)$$

$$C_L = -C_Z \cos \alpha + C_X \sin \alpha \quad (27b)$$

and in the wind axes as

$$C_{D_w} = C_D \cos \beta - C_Y \sin \beta \quad (28a)$$

$$C_{Y_w} = C_Y \cos \beta + C_D \sin \beta \quad (28b)$$

The nondimensional aerodynamic moment coefficients are computed as

$$C_l = \frac{1}{\bar{q}Sb} [I_{xx}\dot{p} - I_{xz}(pq + \dot{r}) + (I_{zz} - I_{yy})qr - L_T] \quad (29a)$$

$$C_m = \frac{1}{\bar{q}S\bar{c}} [I_{yy}\dot{q} + (I_{xx} - I_{zz})pr + I_{xz}(p^2 - r^2) - M_T] \quad (29b)$$

$$C_n = \frac{1}{\bar{q}Sb} [I_{zz}\dot{r} - I_{xz}(\dot{p} - qr) + (I_{yy} - I_{xx})pq - N_T] \quad (29c)$$

where standard simplifying assumptions were assumed [9,19]. The terms  $L_T$ ,  $M_T$ , and  $N_T$  represent moments induced by the propulsion system.

The nondimensional generalized force coefficients driving the vibration modes are calculated by rearranging Eq. (9) as

$$C_{Q_i} = \frac{m_i}{\bar{q}S\bar{c}} [\ddot{\eta}_i + 2\zeta_i\omega_i\dot{\eta}_i + \omega_i^2\Delta\eta_i] \quad (30)$$

and substituting the modal states and modal constants.

At this point, all the relevant modeling data have been obtained, and an equation-error analysis may proceed in either a batch or real-time fashion.

#### IV.F. Practical Aspects

Errors in the measurements and other data used for the estimation impact the accuracy of the aeroelastic stability and control derivatives. Reference [20] investigated how errors in geometry, mass distribution, and flight condition impact the parameter estimates for rigid-body models. For flexible aircraft, the modal parameters and mode shapes can introduce additional errors into the stability and control derivative estimates.

The modal frequencies and damping ratios implemented in the analysis can be modeled as the true value and an error

$$\hat{\omega}_i = \omega_i + \tilde{\omega}_i \quad (31a)$$

$$\hat{\zeta}_i = \zeta_i + \tilde{\zeta}_i \quad (31b)$$

Error in the modal masses  $m_i$  is not considered because in this work the mode shapes were scaled so that the modal masses were unity. Substituting these values into the generalized force coefficients from Eq. (30) results in

$$\hat{C}_{Q_i} = \frac{m_i}{\bar{q}S\bar{c}} [\ddot{\eta}_i + 2\zeta_i\omega_i\dot{\eta}_i + \omega_i^2\eta_i] + \frac{m_i}{\bar{q}S\bar{c}} [2(\zeta_i\tilde{\omega}_i + \tilde{\zeta}_i\omega_i + \tilde{\zeta}_i\tilde{\omega}_i)\dot{\eta}_i + (2\omega_i\tilde{\omega}_i + \tilde{\omega}_i^2)\eta_i] \quad (32)$$

where the first bracketed quantity on the right side is the true value and the second bracketed quantity is a bias. Although excellent fits can be obtained for this data, estimates of the modal parameters

$$\hat{C}_{Q_{i\eta_i}} = C_{Q_{i\eta_i}} + \frac{m_i}{\bar{q}S\bar{c}} [2\omega_i\tilde{\omega}_i + \tilde{\omega}_i^2] \quad (33a)$$

$$\hat{C}_{Q_{i\dot{\eta}_i}} = C_{Q_{i\dot{\eta}_i}} + 2\frac{m_i}{\bar{q}S\bar{c}} [\zeta_i\tilde{\omega}_i + \tilde{\zeta}_i\omega_i + \tilde{\zeta}_i\tilde{\omega}_i] \quad (33b)$$

contain additional terms due to the errors and therefore are biased. Damping ratio errors only bias the modal damping term, whereas damping ratios and frequency errors impact both the modal stiffness and damping. The other parameters are not affected because these errors are proportional to  $\eta_i$  and  $\dot{\eta}_i$ . When assembled into linear state-space models [10], the biases in these estimated derivatives will alter the frequency and damping of the eigenvalues.

Although  $C_{Q_i}$  can be used for estimation, it is preferable to instead use  $\ddot{\eta}_i$  for the reasons just discussed. Rearranging Eq. (9) and expanding in terms of stability and control derivatives, the least-squares problem

becomes

$$\begin{aligned}
\ddot{\eta}_i &= \frac{m_k}{\bar{q}S\bar{c}} C_{Q_i} - \omega_i^2 \Delta\eta_i - 2\zeta_i \omega_i \dot{\eta}_i \\
&= \frac{\bar{q}S\bar{c}}{m_i} \left[ C_{Q_{i_\alpha}} \Delta\alpha + C_{Q_{i_q}} \frac{q\bar{c}}{2V_0} + C_{Q_{i_{\eta_k}}} \Delta\eta_k + C_{Q_{i_{\dot{\eta}_k}}} \frac{\Delta\dot{\eta}_k \bar{c}}{2V_0} + C_{Q_{i_\delta}} \Delta\delta \right]_{k \neq i} \\
&\quad + \left[ \frac{\bar{q}S\bar{c}}{m_i} C_{Q_{i_{\eta_i}}} - \omega_i^2 \right] \Delta\eta_i + \left[ \frac{\bar{q}S\bar{c}}{m_i} C_{Q_{i_{\dot{\eta}_i}}} \frac{\bar{c}}{2V_0} - 2\zeta_i \omega_i \right] \Delta\dot{\eta}_i
\end{aligned} \tag{34}$$

The bracketed terms that multiply  $\Delta\eta_i$  and  $\dot{\eta}_i$  in the above equation are the equivalent  $-\bar{\omega}_i^2$  and  $-2\bar{\zeta}_i \bar{\omega}_i$  terms, which combine the air-off and air-on effects. A similar formulation has been used with output error when FEM data was not available [4, 5]. If the air-off contributions are available from a FEM or GVT, they can be subtracted from these equivalent estimates to obtain the air-on contributions. Performing the estimation in this manner introduces the FEM data at the end of the estimation and stops associated errors from propagating throughout the analysis, as in the case when estimating  $C_{Q_i}$  directly.

Similarly for other computations, measured data should not be altered until it must, to safeguard against propagating errors through the analysis. For example, computing the moment coefficient  $C_m$  requires differentiating the mean-axis pitch rate  $q$ . Now once the Kalman filter produces estimates of  $\dot{\eta}$ , the modal contributions can be subtracted from the gyroscope measurement to yield  $q$ , which could then be differentiated to produce  $\dot{q}$ . However, errors in the estimated  $\dot{\eta}$  will be introduced and magnified in this way, and then will degrade the accuracy of  $C_m$ . These errors will in turn cloud the modeling analysis and will bias the pitching moment derivatives. A more accurate procedure is to first differentiate the measured gyroscope data, and then subtract contributions from  $\ddot{\eta}$ , which are more accurate themselves, to obtain  $\dot{q}$  and  $C_m$ .

Errors in the mode shapes of the vibration modes used to estimate the modal states also affect the analysis. When many sensors are used in this process, the estimates become robust to noise, low excitations, and position errors of the sensors. Although small errors are negligible, large systematic errors in the mode shapes, for example incorrect values for material properties within the FEM, will yield inaccurate basis functions for extracting the modal states and the modal expansion in Eq. (10) will exhibit slower convergence. An analyst may be tempted to compensate by increasing the number of modes included in the estimation, but this action will bias the modal state estimates and supply kinematically inconsistent information to the Kalman filter. Therefore, effort should be made to develop an accurate FEM, and care should be taken in designing experiments and selected modes to include in the analysis.

## V. X-56A Aircraft and Flight Tests

### V.A. Aircraft

The X-56A is a tailless, flying-wing aircraft with swept-back wings. Figure 2 shows a photo of the X-56A flying over NASA Armstrong Flight Research Center. The aircraft has a 28 ft wingspan and weighs between 200 and 480 lbf, depending on fuel, ballast, and configuration. Two JetCat P-400 engines, each capable of providing 90 lbf of thrust, are mounted above the aft section of the center body. The landing gear are arranged in a fixed, tricycle configuration.

The wings have a high aspect ratio and include stationary winglets installed at the wing tips. There are two control surfaces along the trailing edge of the center body, and four control surfaces along the trailing edge of each wing. The ten total control surfaces are used in different combinations to generate aerodynamic control moments, alleviate gust responses, and suppress aeroelastic vibrations.

For more information, Refs. [1, 5, 21–23] describe the conceptual design of the aircraft, NASA research directions, development of the FEM and the GVT experiment, control design, and identification results from flight tests with the stiff-wing configuration.

### V.B. Instrumentation

The X-56A was equipped with a large number of sensors to study its aeroelastic characteristics. A planform of the aircraft showing naming conventions and locations for a subset of the sensors used in this paper is shown in Fig. 3.



Figure 2. X-56A in flight over NASA Armstrong Flight Research Center (credit: NASA / Jim Ross)

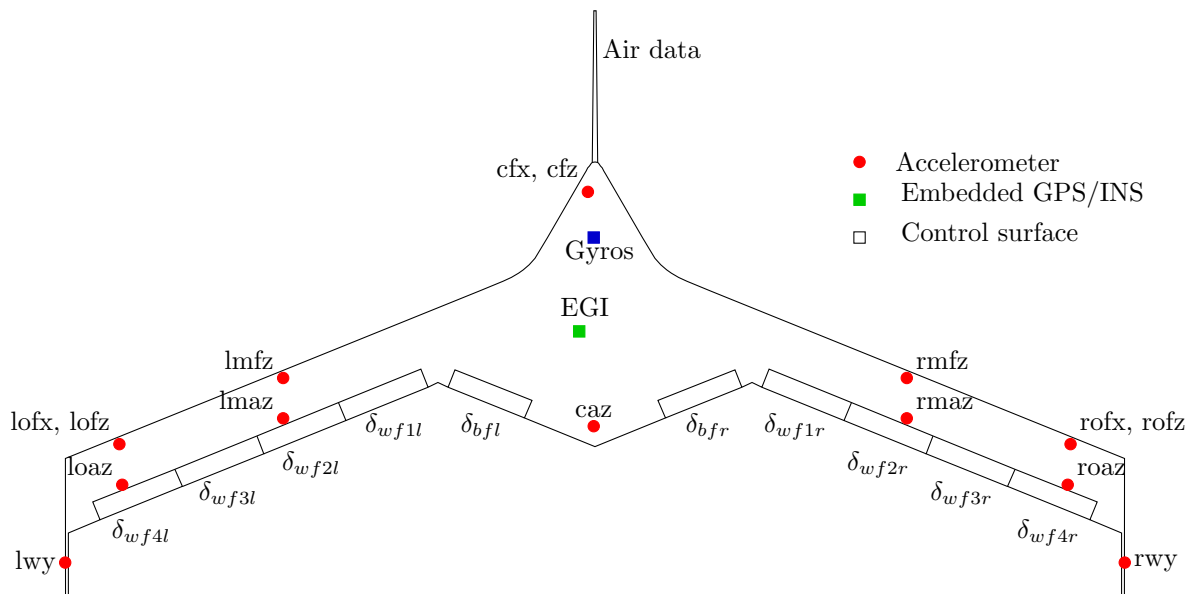


Figure 3. X-56A planform with selected sensor and control surface locations

The trailing-edge control surfaces are first designated with “*bf*” for body flap or “*wf*” for wing flap. The wing flaps are additionally annotated with a number, which increases from wing root to wing tip. The designations end with “*l*” or “*r*” for left or right. All control deflections are considered positive with trailing-edge down deflection. Control surface commands were recorded, as well as measurements from string potentiometers measuring the actual control surface deflections.

The X-56A is instrumented with 18 accelerometers: four longitudinal accelerations, three lateral accelerations, and eleven vertical accelerations. The embedded GPS/INS (EGI) system contains three of these accelerometers, and is located near the nominal center of mass. The center-body and wing accelerometers are designated first with an “*l*” for left wing, “*c*” for center body, or “*r*” for right wing; then “*w*” for winglet, “*o*” for outboard, or “*m*” for midspan; followed by “*f*” for forward, or “*a*” for aft. The last character is “*x*,” “*y*,” or “*z*” and designates the aircraft body axis in which the instrument is aligned.

The EGI also includes three-axis gyroscopes for measuring the body-axis angular rates, and computes Euler angles for the orientation. Additional high-rate gyroscopes are installed in the center body. Air data vanes on the boom protruding from the aircraft nose provided measurements of angle of attack and flank angle. The nose boom also contained pressure ports, which were combined with temperature and pressure sensor readings to compute airspeed. Differential GPS provided position and inertial velocity information.

For strain data, the X-56A is instrumented with 24 strain gauges. These sensors are a combination of bending gauges and rosettes, and are located around the center body and wing root, primarily for computing wing root bending moments. FOSS strands are also installed along both wings but not yet operational for estimation purposes.

A computer-aided design (CAD) model and a FEM [22] of the X-56A were available. Measurements of fuel flow were combined with the CAD model and measured weights to model the aircraft mass, center of mass, and inertia matrix during flight. The FEM was used to tabulate the modal frequencies and the vibration mode shapes at 17 fuel weight cases. GVT data were used to obtain damping ratios for the modes at the full fuel and empty fuel conditions.

## VI. Flight Test Results

This section presents estimation results for one flight test maneuver of the X-56A airplane. For this maneuver, the aircraft was trimmed for straight and level flight at a low angle of attack and nominal altitude. The fuel was at 63% of capacity and the airspeed was at 67% of the predicted flutter boundary. The aircraft was flying with feedback control active; however, the excitation input and the manner in which it was applied enabled the estimation of the open-loop aerodynamic model. The analysis presented here was performed post-flight, but similar analyses could be conducted during flight tests in the future.

Once the airplane was on condition, a set of orthogonal optimized multisine inputs were added to the actuator commands to move the control surfaces as sets of symmetric pairs. These inputs were sums of harmonic sinusoids that contained uniform power to excite the short period and first symmetric vibration mode. Phase angles for the sinusoids were optimized for minimal relative peak factor to elicit small perturbation responses suitable for linear modeling. The harmonic frequencies were allocated to the different control surface pairs in an alternating manner so that each input was orthogonal to the others in both the time and frequency domains. Running these perturbation inputs on multiple control surfaces simultaneously over a frequency bandwidth of interest and with a specified power spectra resulted in excellent aeroelastic modeling data obtained in an efficient manner. For more information on multisine inputs and flight test examples, see Refs. [9, 24].

Control surface deflections for one maneuver are shown in Fig. 4. These time series were computed from potentiometer measurements as

$$\delta_{*s} = \frac{1}{2} (\delta_{*r} + \delta_{*l}) \quad (35)$$

where  $*$  stands for either the body flaps or a pair of wing flaps, and where “*s*” indicates symmetric movement. These inputs appear different from each other and were designed to be orthogonal with pairwise correlation coefficients equal to 0. There is a small amount of control activity in the data, for example a low-frequency oscillation in  $\delta_{bfs}$  to reject the phugoid response, or how  $\delta_{wf2s}$  and  $\delta_{wf3s}$  were ganged together to act as a conventional elevator. However, the highest correlation was 0.15, which is small compared to 0.9 (in absolute value) necessary for accurate modeling [9]. This maneuver was relatively short and incurred a 1.8% change in fuel weight with 0.14% and 0.04% changes in mass and inertia. From analysis with simulation data, these

changes had a negligible effect on the structural dynamics, flight dynamics, and system identification results.

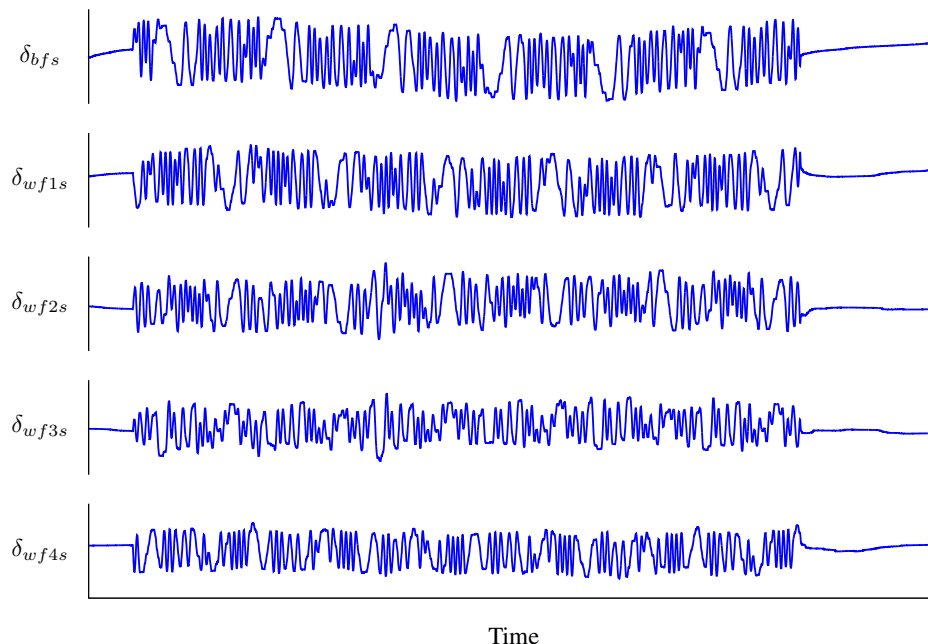


Figure 4. Symmetric control deflections

Measured responses are shown in Fig. 5 for a small subset of the onboard sensors. The responses were low in amplitude but had good signal-to-noise ratios. Airspeed and dynamic pressure varied less than 1.2% and 1.9% from the reference values, respectively, and was approximated as constants in the analysis. Using spectral analysis, it was observed that the apparent higher noise levels in  $a_z^{roaz}$  (sensor installed near the wingtip) relative to  $a_z^{egi}$  (sensor installed near the mass center) was due to the presence of many higher-frequency structural modes in the data. The frequency spectrum for this measurement is shown in Fig. 6 with annotations for the corresponding FEM vibration mode numbers (mentioned next) and general ranges.

For the analysis of this maneuver, five vibration modes were significant. These mode shapes are depicted in Fig. 7 using the FEM data, where the gray and black markers represent the undeformed and deformed aircraft, respectively. The deformations shown are exaggerated to different degrees for each mode to help convey the mode shape. The mode numbering corresponded to the FEM, where the first six modes were the rigid-body degrees of freedom. Mode 7 is the first symmetric wing bending (SW1B) mode, where the wings and nose bend down while the aft section of the center body bends up. Mode 8 is the anti-symmetric first bending (AW1B) mode, where the wings bend in opposite directions and the centerbody rolls to one side. Mode 9 is the first symmetric wing torsion (SW1T) mode and includes symmetric twisting of the wings. Mode 10 is the symmetric wing fore-aft (SWFA) mode, wherein the wings bend forwards and backwards. Mode 14 is the symmetric winglet lateral (SWL) mode and involves a symmetric lateral bending of the winglets in addition to first bending and first torsion of the wings, as well as first vertical bending of the airdata boom. Many other modes were evident in the flight test data but did not significantly impact this analysis and were therefore not estimated. The neglected modes 11–13 over this bandwidth are the first anti-symmetric torsion, and both symmetric and anti-symmetric vibrations of the main landing gear. The multisine inputs used in this maneuver were intended to only excite the short period and SW1B modes; the presence of the other modes are due to other sources that may include aeroelastic coupling, pilot and control law inputs, ambient turbulence, and initiation or cessation of the excitation inputs.

The accelerometer data were first examined. Estimated time histories and frequency spectra for  $C_Z$  and  $\ddot{\eta}$  are shown in Fig. 8. The  $C_X$  and  $C_Y$  coefficients were also estimated but are not shown because the  $C_Z$  coefficient was of primary interest in this paper. Additionally, the uncertainty estimates are not shown in Fig. 8(a) for clarity. A different  $y$ -axis range is used on each plot so that signals can be distinguished. However,  $C_Z$  and  $\ddot{\eta}_7$  were much larger in amplitude than the other modal accelerations because these multisine inputs were designed to excite the short period and SW1B modes, although other resonances are present in the data. If these additional modes (AW1B, SW1T, SWFA, and SWL) were not included in the estima-

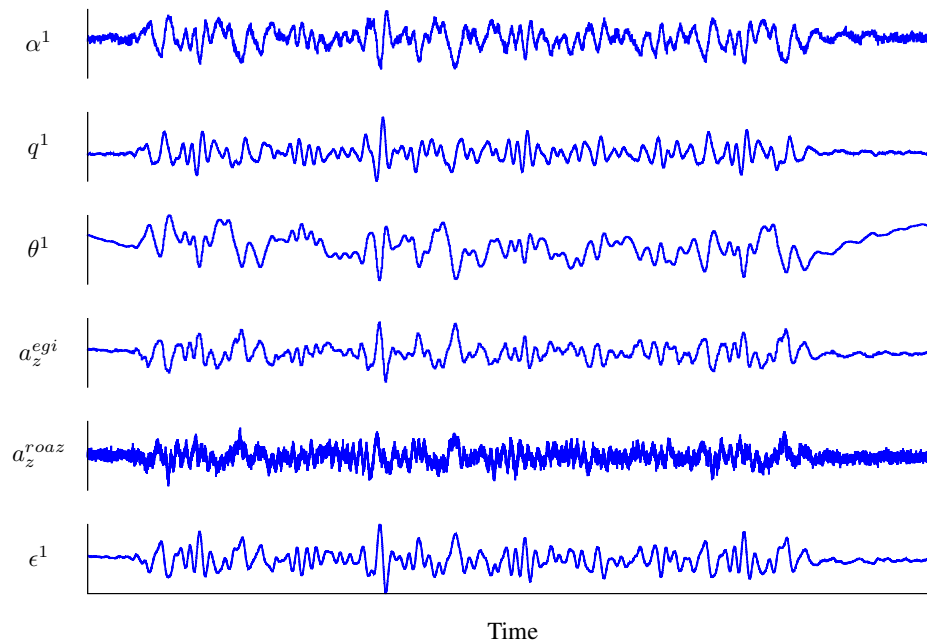


Figure 5. Measurements from a subset of onboard sensors

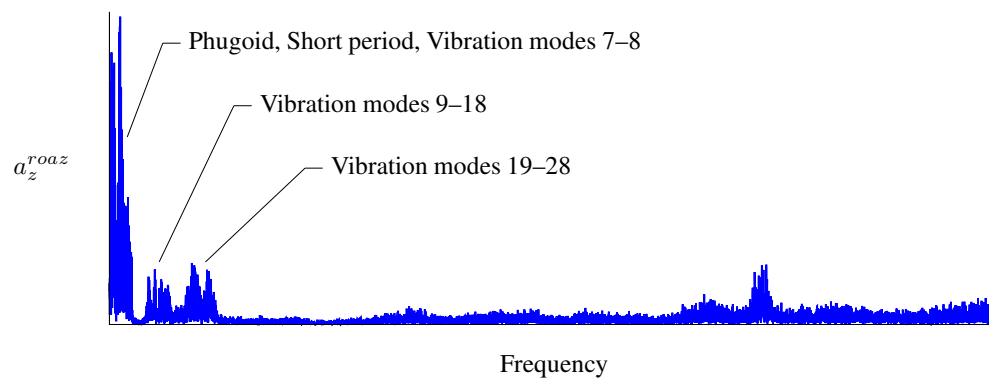
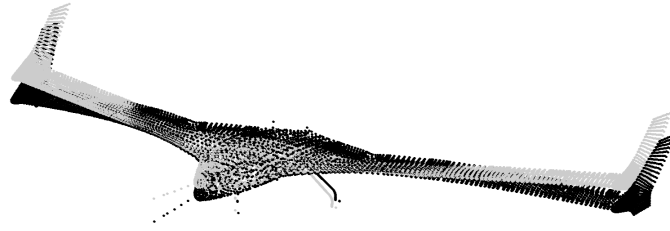
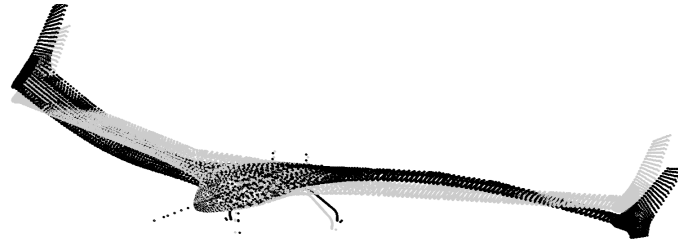


Figure 6. Spectrum of accelerometer data

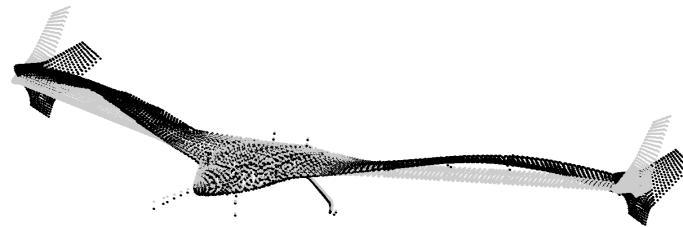




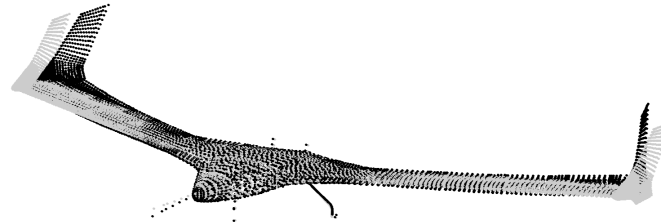
(a) Mode 7: first symmetric wing bending (SW1B)



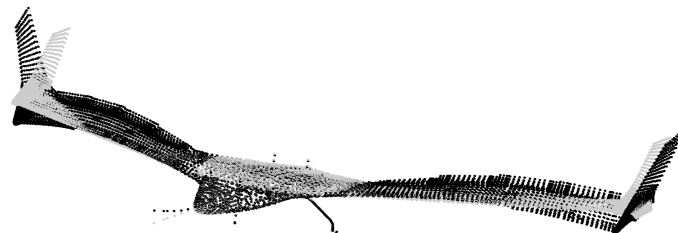
(b) Mode 8: first anti-symmetric wing bending (AW1B)



(c) Mode 9: first symmetric wing torsion (SW1T)



(d) Mode 10: symmetric wing fore-aft (SWFA)



(e) Mode 14: symmetric winglet lateral (SWL)

**Figure 7.** Mode shapes for the X-56A (FEM configuration 24611, version 10.424\_dev, 50% fuel) — gray markers are the undeformed grid points and black markers are the corresponding deformed points

tion, their contributions would be attributed to other retained signals in the least-squares estimation. These modes were much more important for the strain data, discussed next, than the accelerometer data. As shown in Fig. 8(b), the vibration modes have resonances that are separated in frequency, but also have significant responses at other frequencies, especially the lower frequencies. The higher-frequency content in the  $\ddot{\eta}_8$  estimates is due to the asymmetric wing first torsion mode; however there was not enough data information to accurately extract this mode. Coefficients of determination  $R^2$  quantifying fits to relevant accelerometer data (not shown) ranged between 0.92 to 0.98, indicating excellent fits to the measured accelerometer data. The small errors are attributed to neglected higher-frequency vibrations and to measurement noise. Examination of the regressor matrix  $\mathbf{X}$  formed using Eq. (25) indicated that it was well-conditioned and that explanatory variables had low pairwise correlations.

The strain data were next examined. Because strain sensors register only modal displacements, they are more sensitive to neglected structural modes than the accelerometers. It was for this reason that several higher-frequency modes were needed to obtain accurate modal displacement estimates. Time histories and frequency spectra for  $\eta$  estimates are shown in Fig. 9. Again the axes in these plots are scaled to distinguish between the signals, rather than for comparing their amplitudes, and the SW1B mode is significantly larger than the other modes due to the input excitation. Because the excitation was relatively low in frequency but many higher-frequencies are present in the data, the higher-frequency modal displacements are significantly correlated with the bending mode, as can be seen from Fig. 9. This had an impact on modeling and is discussed later. Values of  $R^2$  for the measured and modeled strain data were between 0.72 and 0.98, which indicated good fits. The correlation matrix from Eq. (15) was well-conditioned and no significant correlations among the data were observed.

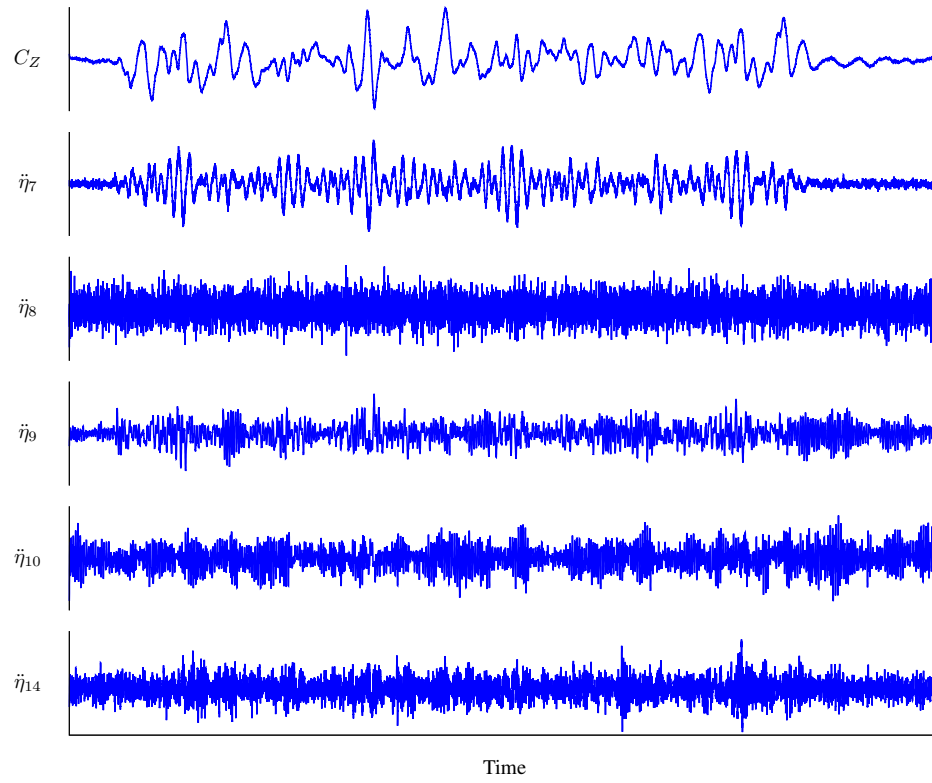
The Kalman filter estimated modal displacements, rates, and accelerations from the estimated modal displacement and acceleration data just discussed. Only one set of airdata measurements were available and although there were two gyroscopes, one was recorded at a slower rate and did not contain significant contributions from the vibrations. Consequently, modal rates were not initially estimated using least squares, but were available as outputs from the Kalman filter. Relatively small adjustments were made by the filter to the original modal displacement data.

An examination of the estimated explanatory variables indicated that  $\alpha$  was highly correlated with the  $\eta_9$ ,  $\eta_{10}$ , and  $\eta_{14}$ . This was because the SW1T, SWFA, and SWL modes have a low-frequency coupling with  $\alpha$ , but the higher-frequency resonances were not sufficiently excited to lower the correlations. In other maneuvers that excited these higher-frequency modes, these correlations were significantly lower. Although the SW1B mode was specifically targeted in this maneuver, the correlation of  $\alpha$  and  $\eta_7$  was still 0.85. This was to be expected because the SW1B mode is lightly damped and the forcing from  $\alpha$  was lower in frequency, where the dynamics are passed without much gain and phase distortion. As a result of these correlations, only the short period and SW1B modes were modeled for parameter estimation, and the only modal states used as explanatory variables were  $\eta_7$  and  $\dot{\eta}_7$ . This, however, was the original intention for this maneuver. Figure 10 illustrates pairwise correlations for the retained regressors. Except as already discussed, pairwise correlations were not significant.

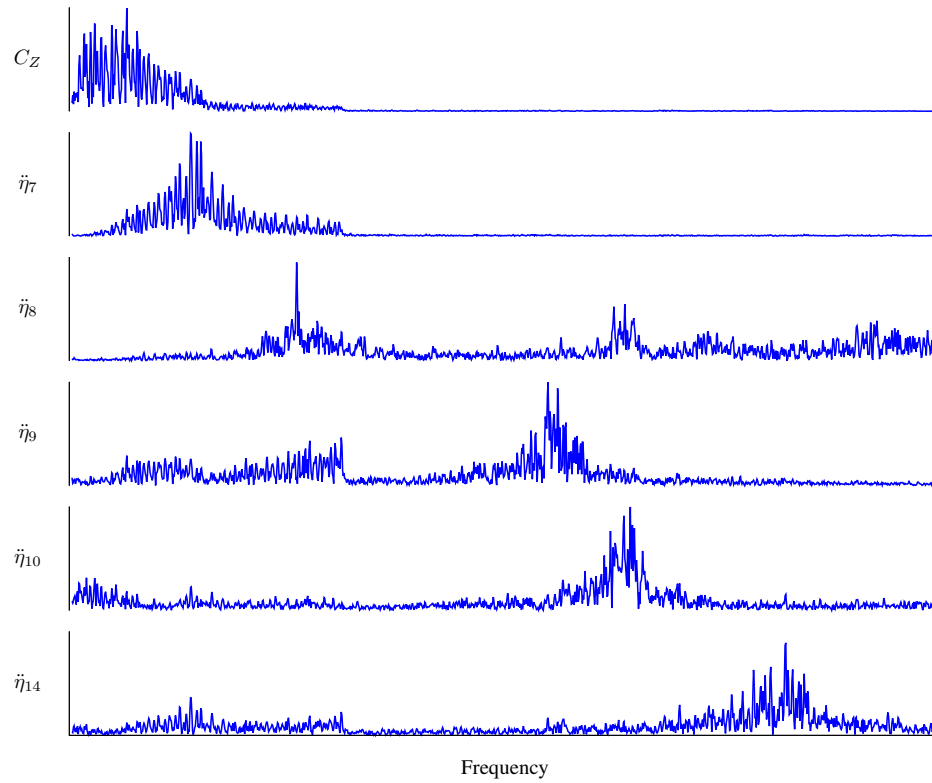
Dependent modeling data and model fits to that data in the frequency domain are shown in Fig. 11 using the entire maneuver record. For comparison and discussed more next, fits to both  $C_{Q_7}$  and  $\ddot{\eta}_7$  are shown. The fits ranged in  $R^2$  from 0.96 to 0.97, indicating an excellent fit. Minor errors in the lowest frequencies for  $C_L$  and  $C_{Q_7}$  are due to phugoid excitation, as corroborated by the low-frequency oscillation in the inboard flaps seen in Fig. 4.

Estimated stability and control derivatives are shown in Fig. 12 with  $2\sigma$  uncertainty ranges. For comparison, predictions obtained using the ZAERO software for the 50% fuel case [25] are shown in green. Values generally agreed between the predicted and identified values, although there are discrepancies, particularly in the  $q$  derivatives. The term  $C_{L_q}$ , is not typically estimated at low angles of attack because it is small with low sensitivity. The same derivatives for  $C_{Q_7}$  are shown from both  $C_{Q_7}$  data and  $\ddot{\eta}_7$  data. These values differed less than 1%, which indicated that the FEM and the reconstructions of  $\eta_7$  and  $\dot{\eta}_7$  did not contain significant error for the SW1B mode.

Real-time estimates obtained using the recursive Fourier transform and equation error in the frequency domain are shown for a few parameters in Fig. 13 with  $2\sigma$  uncertainties. Estimates began soon after the excitation started, and were computed at regular intervals. In the beginning of the maneuver, the parameter estimates vary wildly and had larger uncertainties. As more information was recorded, the estimates quickly converged near their final values, shown in Fig. 12.

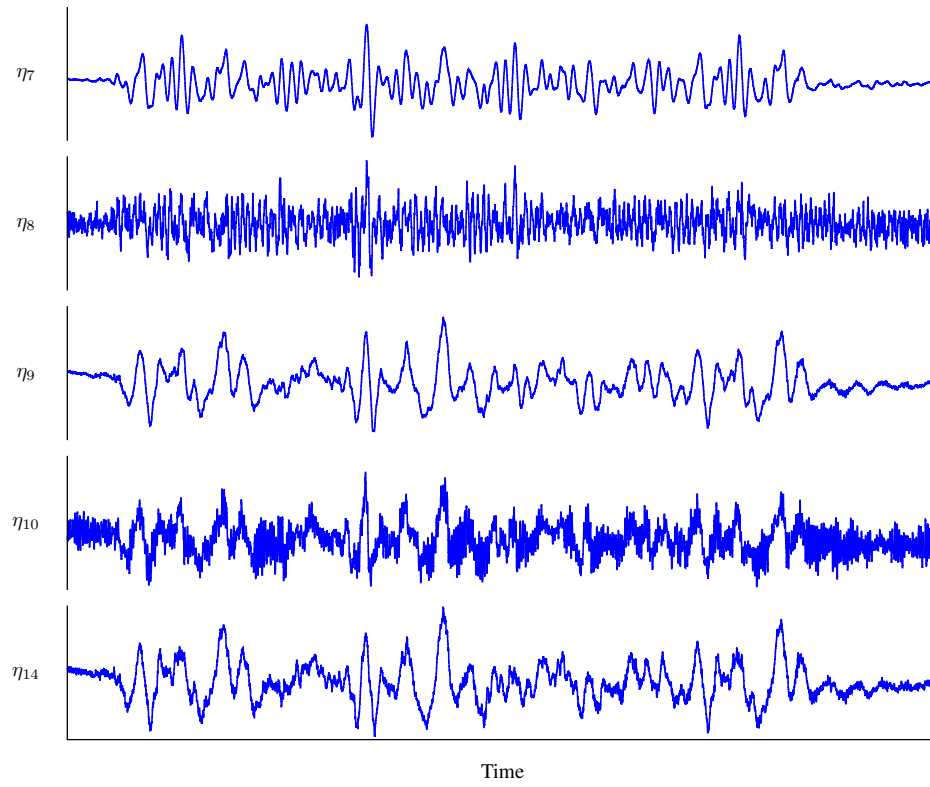


(a) Time histories

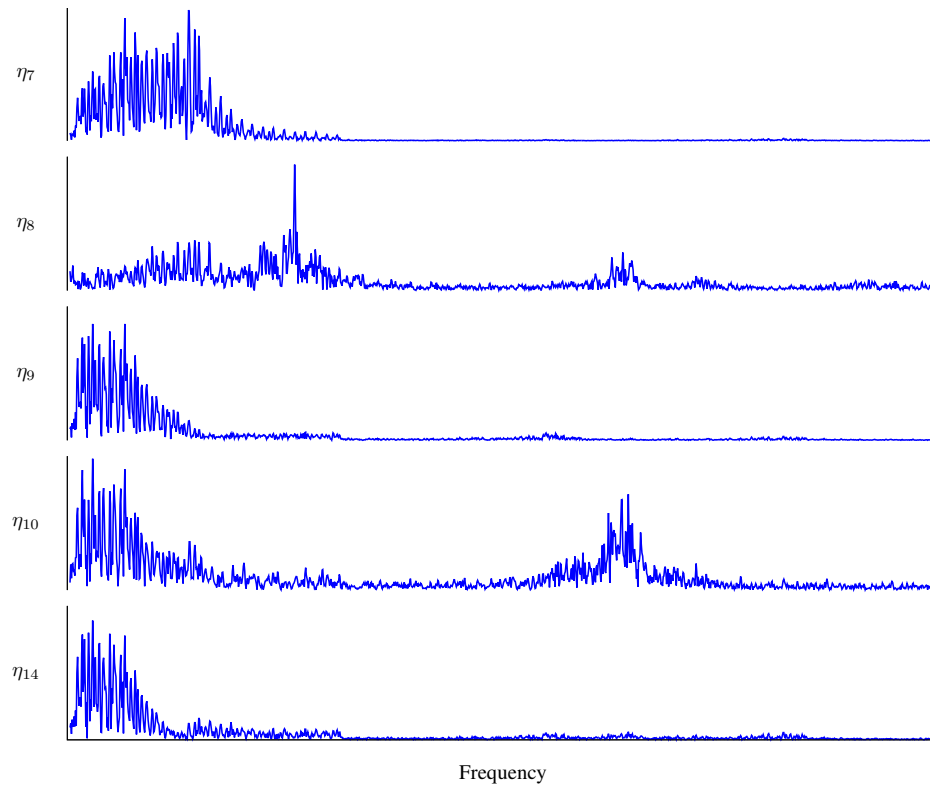


(b) Fourier transforms

Figure 8. Estimated vertical force coefficient and modal accelerations from accelerometer and gyroscope data



(a) Time histories



(b) Fourier transforms

**Figure 9. Estimated modal displacements from strain data**

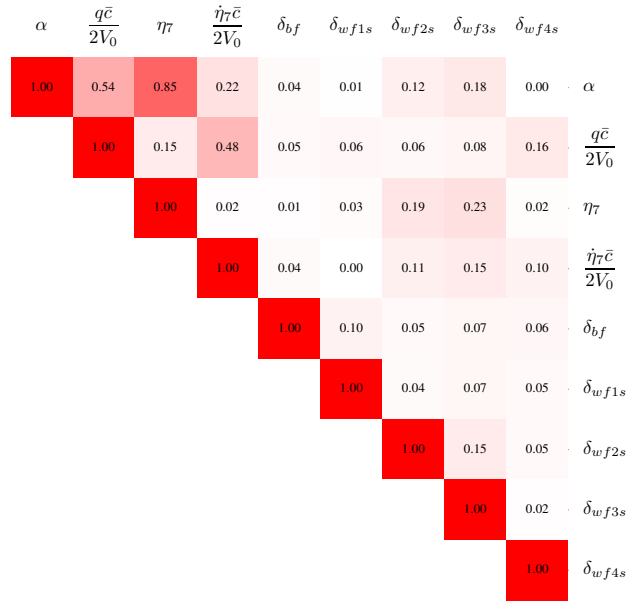


Figure 10. Pairwise correlation magnitudes for the retained explanatory variables

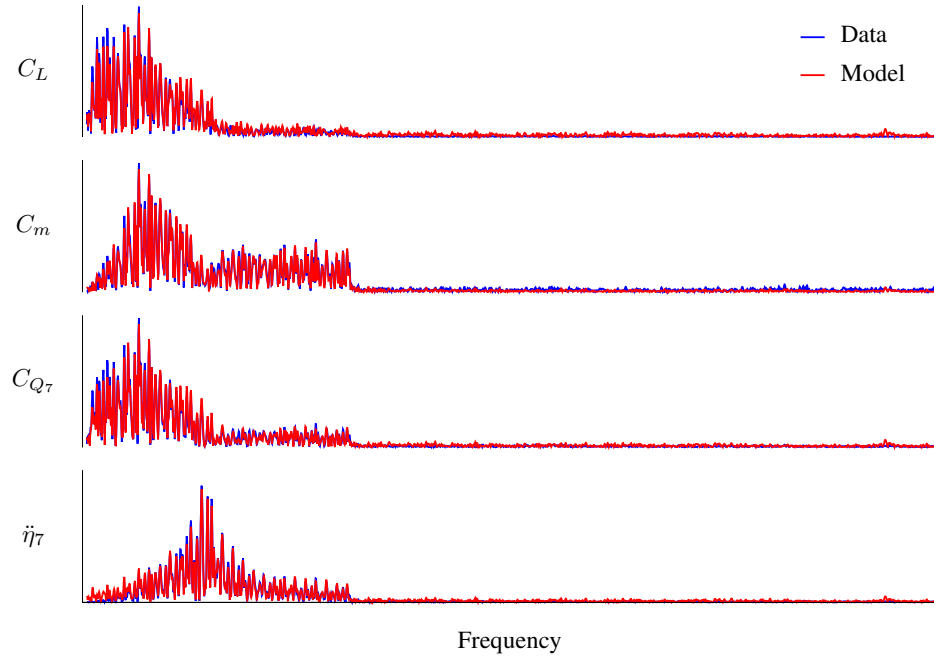


Figure 11. Model fits to frequency-domain data

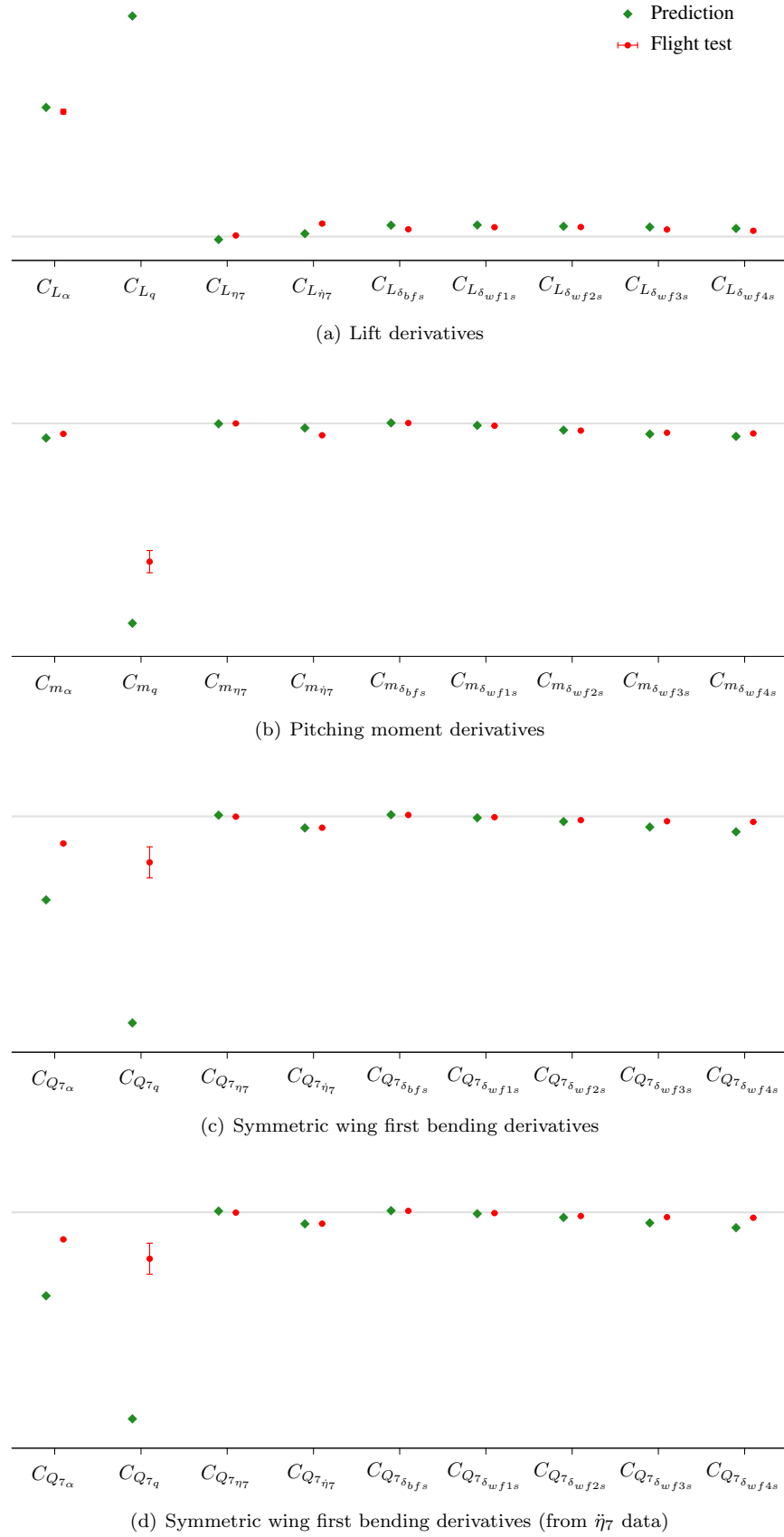


Figure 12. Stability and control derivative estimates from numerical prediction and from flight test data

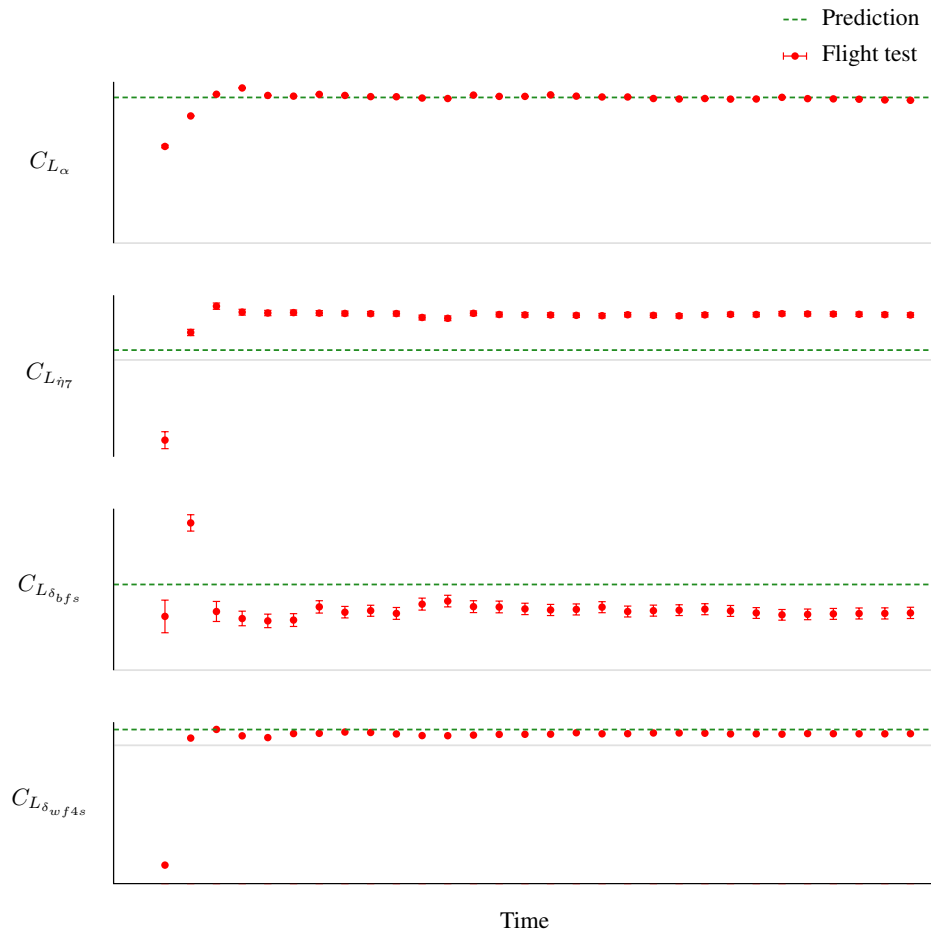


Figure 13. Real-time estimates for a subset of parameters

To illustrate the identified dynamics, the estimated stability and control derivatives were assembled with other data into a linear state-space model of the form

$$\begin{bmatrix} \dot{\alpha} \\ \dot{q} \\ \dot{\eta}_7 \\ \ddot{\eta}_7 \end{bmatrix} = \begin{bmatrix} -\frac{\bar{q}S}{mV}C_{L\alpha} & 1 - \frac{\bar{q}S}{mV}\frac{\bar{c}}{2V}C_{Lq} & -\frac{\bar{q}S}{mV}C_{L\eta_7} & -\frac{\bar{q}S}{mV}\frac{\bar{c}}{2V}C_{L\dot{\eta}_7} \\ \frac{\bar{q}S\bar{c}}{I_{yy}}C_{m\alpha} & \frac{\bar{q}S\bar{c}}{I_{yy}}\frac{\bar{c}}{2V}C_{mq} & \frac{\bar{q}S\bar{c}}{I_{yy}}C_{m\eta_7} & \frac{\bar{q}S\bar{c}}{I_{yy}}\frac{\bar{c}}{2V}C_{m\dot{\eta}_7} \\ 0 & 0 & 0 & 1 \\ \frac{\bar{q}S\bar{c}}{m_7}C_{Q_{\tau\alpha}} & \frac{\bar{q}S\bar{c}}{m_7}\frac{\bar{c}}{2V}C_{Q_{\tau q}} & \frac{\bar{q}S\bar{c}}{m_7}C_{Q_{\tau\eta_7}} - \omega_7^2 & \frac{\bar{q}S\bar{c}}{m_7}\frac{\bar{c}}{2V}C_{Q_{\tau\dot{\eta}_7}} - 2\zeta_7\omega_7 \end{bmatrix} \begin{bmatrix} \Delta\alpha \\ \Delta q \\ \Delta\eta_7 \\ \Delta\dot{\eta}_7 \end{bmatrix} \\ + \begin{bmatrix} -\frac{\bar{q}S}{mV}C_{L\delta_{bf}s} & -\frac{\bar{q}S}{mV}C_{L\delta_{wf1}s} & -\frac{\bar{q}S}{mV}C_{L\delta_{wf2}s} & -\frac{\bar{q}S}{mV}C_{L\delta_{wf3}s} & -\frac{\bar{q}S}{mV}C_{L\delta_{wf4}s} \\ \frac{\bar{q}S\bar{c}}{I_{yy}}C_{m\delta_{bf}} & \frac{\bar{q}S\bar{c}}{I_{yy}}C_{m\delta_{wf1}} & \frac{\bar{q}S\bar{c}}{I_{yy}}C_{m\delta_{wf2}} & \frac{\bar{q}S\bar{c}}{I_{yy}}C_{m\delta_{wf3}} & \frac{\bar{q}S\bar{c}}{I_{yy}}C_{m\delta_{wf4}} \\ 0 & 0 & 0 & 0 & 0 \\ \frac{\bar{q}S\bar{c}}{m_7}C_{Q_{\tau\delta_{bf}}} & \frac{\bar{q}S\bar{c}}{m_7}C_{Q_{\tau\delta_{wf1}}} & \frac{\bar{q}S\bar{c}}{m_7}C_{Q_{\tau\delta_{wf2}}} & \frac{\bar{q}S\bar{c}}{m_7}C_{Q_{\tau\delta_{wf3}}} & \frac{\bar{q}S\bar{c}}{m_7}C_{Q_{\tau\delta_{wf4}}} \end{bmatrix} \begin{bmatrix} \Delta\delta_{bf} \\ \Delta\delta_{wf1} \\ \Delta\delta_{wf2} \\ \Delta\delta_{wf3} \\ \Delta\delta_{wf4} \end{bmatrix} \quad (36)$$

It is important to note that coupling terms for aeroelastic aircraft models can be significant and truncating the model, as in Eq. (36), can significantly affect the dynamics [10, 26]. As illustrated by the selected Bode magnitudes shown in Fig. 14, the eigenvalues of the system represented two oscillatory modes with low damping. Phasor diagrams illustrating the eigenvectors for the two modes are shown in Fig. 15. Although the normal relationship between  $\alpha$  and  $q$  is present in the short period mode,  $\eta_7$  and  $\dot{\eta}_7$  participate significantly in the response. This underscores that the traditional rigid-body modes are still present for flexible aircraft, but are now coupled with the structural degrees of freedom. The SW1B mode is mostly the oscillation in  $\dot{\eta}_7$ , but also contains terms from the other states.

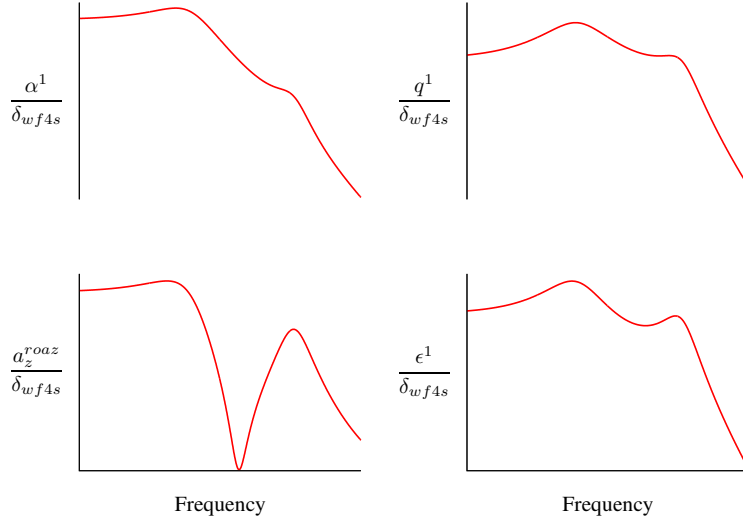
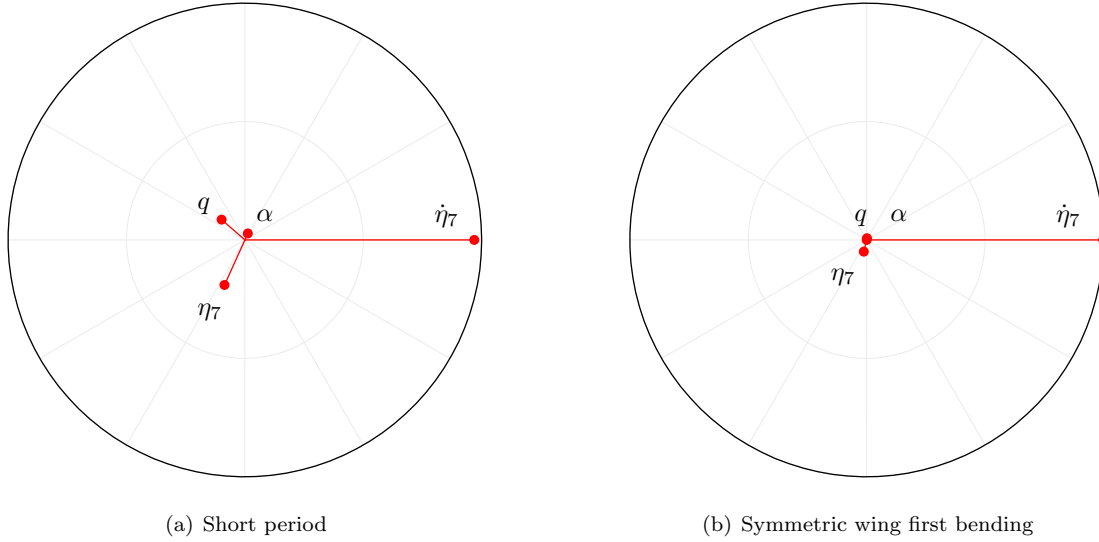


Figure 14. Subset of Bode magnitude plots from the identified model

## VII. Conclusions

This paper presented a method for performing batch or real-time parameter estimation for flexible aircraft. Knowledge of the air-off, in-vacuo mode shapes was leveraged to estimate displacements, rates, and accelerations of generalized modal coordinates, as well as nondimensional aerodynamic force coefficients, from onboard sensor measurements using least squares. Kinematic consistency was enforced using a Kalman filter, which improved the modeling data. Modeling variables were then computed and applied to parameter estimation using equation error in the frequency domain, which can be applied in a post-flight or real-time framework. This method was demonstrated with flight test data for the X-56A aeroelastic demonstrator flying under closed-loop control, and had good results for the short period and symmetric wing first bending modes, which were similar to previous numerical predictions.





**Figure 15. Phasor diagrams using eigenvectors from the identified model**

The cost to use this method is the extra analyses required to develop an accurate FEM for calculating mode shapes and modal constants. This requirement is in addition to obtaining accurate values for standard mass and geometry parameters, such as the inertia tensor. Afterwards, numerous redundant sensors, specifically strain sensors and accelerometers, are needed to observe the modes of interest. Extra computing power is also needed to process all the data and at faster sampling rates than typically used for traditional aircraft. Due to the complexity of the method, there is a sensitivity to errors in the specified mode shapes and other parameters that requires a careful analysis.

However, this method enables many statistical tools for determining model structure and diagnosing data problems. In addition, accurate parameter estimates are computed quickly without iteration or the need for starting values. Previously, modeling for flexible aircraft was restricted to output-error techniques because the generalized modal displacements, rates, and accelerations were not directly measured, resulting in laborious analyses. This analysis can help shorten flight tests or can be run continuously to update flutter predictions. In addition, the modal estimation technique used here can be implemented in real time for modal-based control designs to alleviate gusts and suppress flutter.

## Acknowledgments

This research was supported by the NASA Advanced Air Transport Technology Project. The efforts of the X-56A team at NASA Armstrong Flight Research Center are gratefully acknowledged. Numerical predictions of stability and control derivatives were supplied by Jeffrey Ouellette. Discussions with Jeffrey Ouellette, Chris Miller, Jacob Schaefer, and the other X-56A team members improved the quality of this method and paper, and are appreciated.

## References

- <sup>1</sup>Ryan, J., Bosworth, J., Burken, J., and Suh, P., “Current and Future Research in Active Control of Lightweight, Flexible Structures Using the X-56 Aircraft,” 52nd Aerospace Sciences Meeting, AIAA, National Harbor, MD, January 2014.
- <sup>2</sup>Livne, E., “Aircraft Active Flutter Suppression: State of the Art and Technology Maturation Needs,” *Journal of Aircraft*, Vol. 55, No. 1, January-February 2018, pp. 410–450.
- <sup>3</sup>Theodore, C., Ivler, C., Tischler, M., Field, E., Neville, R., and Ross, H., “System Identification of Large Flexible Transport Aircraft,” No. 2008-6894 in Atmospheric Flight Mechanics Conference, AIAA, Honolulu, HI, August 2008.
- <sup>4</sup>de Oliveira Silva, B. G. and Mönnich, W., “System Identification of Flexible Aircraft in Time Domain,” No. 2012-4412 in AIAA Atmospheric Flight Mechanics Conference, AIAA, Minneapolis, MN, August 2012.
- <sup>5</sup>Grauer, J. and Boucher, M., “Aeroelastic Modeling of the X-56A Stiff-Wing Configuration Flight Test Data,” No. 2017-0699 in Atmospheric Flight Mechanics Conference, AIAA, Grapevine, TX, January 2017.
- <sup>6</sup>Danowsky, B., Schmidt, D., and Pfifer, H., “Control-Oriented System and Parameter Identification of a Small Flexible Flying-Wing Aircraft,” No. 2017-1394 in Atmospheric Flight Mechanics Conference, AIAA, Grapevine, TX, January 2017.
- <sup>7</sup>Waszak, M. and Schmidt, D., “Flight Dynamics of Aeroelastic Vehicles,” *Journal of Aircraft*, Vol. 25, No. 6, June 1988, pp. 563–571.
- <sup>8</sup>Maine, R. and Iliff, K., “Application of Parameter Estimation to Aircraft Stability and Control: the Output-Error Approach,” Tech. Rep. RP-1168, NASA, Edwards, CA, June 1986.
- <sup>9</sup>Morelli, E. and Klein, V., *Aircraft System Identification: Theory and Practice*, Sunflyte, 2016.
- <sup>10</sup>Schmidt, D., *Modern Flight Dynamics*, McGraw-Hill, New York, 2012.
- <sup>11</sup>Grauer, J., “Summary of Output Measurement Equations for Flight Dynamics of Flexible Aircraft,” Tech. rep., NASA, Hampton, VA, 2018, awaiting publication.
- <sup>12</sup>Morelli, E., “System Identification Programs for AirCRAFT (SIDPAC),” <http://software.nasa.gov>, Accessed: 2018–05–16.
- <sup>13</sup>Klein, V., “Parameter Estimation in Frequency Domain,” No. 78-1344 in Atmospheric Flight Mechanics Conference, AIAA, Palo Alto, CA, August 1978, pp. 140–147.
- <sup>14</sup>Morelli, E., “Real-Time Parameter Estimation in the Frequency Domain,” *Journal of Guidance, Control, and Dynamics*, Vol. 23, No. 5, September–October 2000, pp. 812–818.
- <sup>15</sup>Chan, H., Parker, A., Piazza, A., and Richards, W., “Fiber-optic sensing system: Overview, development and deployment in flight at NASA,” 2015 IEEE Avionics and Vehicle Fiber-Optics and Photonics Conference, Nov 2015, pp. 71–73.
- <sup>16</sup>Gelb, A., editor, *Applied Optimal Estimation*, MIT Press, Cambridge, MA, 1974.
- <sup>17</sup>Klein, V. and Schiess, J., “Compatibility Check of Measured Aircraft Responses Using Kinematic Equations and Extended Kalman Filter,” Tech. Rep. TN D-8514, NASA, Hampton, VA, August 1977.
- <sup>18</sup>Grauer, J. and Boucher, M., “Frequency-Domain Deconvolution for Flight Dynamics Applications,” No. 2018-xxxx in Atmospheric Flight Mechanics Conference, AIAA, Atlanta, GA, June 2018.
- <sup>19</sup>McRuer, D., Ashkenas, I., and Graham, D., *Aircraft Dynamics and Automatic Control*, Princeton University Press, 1973.
- <sup>20</sup>Grauer, J. and Morelli, E., “Dependence of Dynamic Modeling Accuracy on Sensor Measurements, Mass Properties, and Aircraft Geometry,” Tech. Rep. TM-2013-218056, NASA, Hampton, VA, November 2013.
- <sup>21</sup>Baranek, J., Nicolai, L., Buonanno, M., Atkinson, C., Holm-Hansen, B., and Flick, P., “Conceptual Design of a Multi-utility Aeroelastic Demonstrator,” No. 2010-9350 in Multidisciplinary Analysis Optimization Conference, AIAA, Fort Worth, TX, September 2010.
- <sup>22</sup>Pak, C. and Truong, S., “Creating a Test-Validated Finite-Element Model of the X-56A Aircraft Structure,” *Journal of Aircraft*, Vol. 52, No. 5, September–October 2015, pp. 1644–1667.
- <sup>23</sup>Suh, P., “Robust Modal Filtering and Control of the X-56A Model with Simulated Fiber Optic Sensor Failures,” No. 2014-2053 in Atmospheric Flight Mechanics Conference, AIAA, Atlanta, GA, June 2014.
- <sup>24</sup>Morelli, E., “Flight Test Maneuvers for Efficient Aerodynamic Modeling,” *Journal of Aircraft*, Vol. 49, No. 6, November–December 2012, pp. 1857–1867.
- <sup>25</sup>Ouellette, J., “Aeroelastic Modeling of Body Freedom Flutter for Control System Design,” No. 2017-0019 in Atmospheric Flight Mechanics Conference, AIAA, Grapevine, TX, January 2017.
- <sup>26</sup>Schmidt, D., “MATLAB-Based Flight-Dynamics and Flutter Modeling of a Flexible Flying-Wing Research Drone,” *Journal of Aircraft*, Vol. 53, No. 4, July–August 2016, pp. 1045.